

Partial Sum Minimization of Singular Values in Robust PCA: Algorithm and Applications

Tae-Hyun Oh *Student Member, IEEE*, Yu-Wing Tai *Senior Member, IEEE*,
Jean-Charles Bazin *Member, IEEE*, Hyeonwoo Kim *Student Member, IEEE*,
and In So Kweon *Member, IEEE*

Abstract—Robust Principal Component Analysis (RPCA) via rank minimization is a powerful tool for recovering underlying low-rank structure of clean data corrupted with sparse noise/outliers. In many low-level vision problems, not only it is known that the underlying structure of clean data is low-rank, but the exact rank of clean data is also known. Yet, when applying conventional rank minimization for those problems, the objective function is formulated in a way that does not fully utilize a priori target rank information about the problems. This observation motivates us to investigate whether there is a better alternative solution when using rank minimization. In this paper, instead of minimizing the nuclear norm, we propose to minimize the partial sum of singular values, which implicitly encourages the target rank constraint in rank minimization. Our experimental analyses show that, when the number of samples is deficient, our approach leads to a higher success rate than conventional rank minimization, while the solutions obtained by the two approaches are almost identical when the number of samples is more than sufficient. We apply our approach to various low-level vision problems, e.g. high dynamic range imaging, motion edge detection, photometric stereo, image alignment and recovery, and show that our results outperform those obtained by the conventional nuclear norm rank minimization method.

Index Terms—Robust principal component analysis, rank minimization, sparse and low-rank decomposition, truncated nuclear norm, alternating direction method of multipliers.



1 INTRODUCTION

Various low-level vision applications, including High Dynamic Range (HDR) [35], [36], photometric stereo [4], [25], batch image alignment [38] and factorization-based structure from motion [6], [41], can be formulated into a low-rank matrix recovery problem. Low-rank matrix approximation methods, such as Principal Component Analysis (PCA) [31] and Matrix Factorization (MF) [8], [20], [40], [49] are widely used to find the best approximation of an underlying low-rank structure of data. However many of these approaches are error-prone due to the presence of outliers. To recover the low-rank matrix while rejecting outliers, a rank minimization based Robust Principal Component Analysis (RPCA) [10] has been proposed and gained much interests in computer vision [30], [38], [46], [48].

RPCA [10] aims to recover a low-rank matrix $\mathbf{A} \in \mathbb{R}^{m \times n}$ from corrupted observations $\mathbf{O} = \mathbf{A} + \mathbf{E}$, where $\mathbf{E} \in \mathbb{R}^{m \times n}$ represents errors with arbitrary magnitude and distribution. The rank minimization approach [10], [11], [39], [43] assumes \mathbf{E} is sparse and formulates the

problem as:

$$\min_{\mathbf{A}, \mathbf{E}} \text{rank}(\mathbf{A}) + \lambda \|\mathbf{E}\|_0, \quad \text{s.t. } \mathbf{O} = \mathbf{A} + \mathbf{E}, \quad (1)$$

where $\|\cdot\|_0$ denotes the l^0 -norm, and λ is the relative weight between the two terms. Unfortunately, solving the problem in Eq. (1) is an NP-hard problem. The rank minimization approaches instead solve an approximated problem by convex surrogate as:

$$\arg \min_{\mathbf{A}, \mathbf{E}} \|\mathbf{A}\|_* + \lambda \|\mathbf{E}\|_1, \quad \text{s.t. } \mathbf{O} = \mathbf{A} + \mathbf{E}, \quad (2)$$

where $\|\mathbf{A}\|_* = \sum_i \sigma_i(\mathbf{A})$ is the nuclear norm of \mathbf{A} , $\sigma_i(\mathbf{A})$ represents the i -th singular value of \mathbf{A} (sorted in decreasing order), and $\|\mathbf{E}\|_1$ is the l^1 -norm of \mathbf{E} . Eq. (2) can be solved effectively by various methods [33], [44]. Wright *et al.* [43] and Candès *et al.* [10] proved that, under mild conditions, the unique solution of Eq. (2) *exactly* corresponds to the solution of the original NP-hard problem in Eq. (1). Yet, when the number of observations in \mathbf{O} is very limited, experiments show that the converged solution includes some outliers as inliers and vice versa. Such limited number of observations are not uncommon in many computer vision problems due to practical reasons. For example, in HDR context, often only 2-4 differently exposed images are captured and photometric stereo requires only 3 images in theory. Moreover, we also observe that the converged solution can be degenerated. For instance, in the photometric stereo problem [46], the solution of \mathbf{A} might have a rank lower than the theoretical rank of 3.

- T.-H. Oh, Y.-W. Tai, H. Kim and I.S. Kweon are with the Department of Electrical Engineering, KAIST, Daejeon, Republic of Korea. I.S. Kweon is the corresponding author.
E-mail: thoh.kaist.ac.kr@gmail.com, yuwing@gmail.com, hyeongwoo.kim@rcv.kaist.ac.kr, iskweon77@kaist.ac.kr
- J.-C. Bazin is with Computer Graphics Laboratory and Computer Vision and Geometry Group, ETH Zürich, Switzerland.
E-mail: jebazin@inf.ethz.ch

In this paper, based on the prior knowledge about the rank of \mathbf{A} , we propose an alternative objective function which minimizes the Partial Sum of Singular Values (abbreviated to PSSV) of \mathbf{A} :

$$\arg \min_{\mathbf{A}, \mathbf{E}} \|\mathbf{A}\|_{p=N} + \lambda \|\mathbf{E}\|_1, \quad \text{s.t. } \mathbf{O} = \mathbf{A} + \mathbf{E}, \quad (3)$$

where $\|\mathbf{A}\|_p = \sum_{i=p+1}^{\min(m,n)} \sigma_i(\mathbf{A})$ and N is the target rank of \mathbf{A} which can be derived from problem definition, e.g. $N = 1$ for background subtraction, $N = 3$ for photometric stereo. Eq. (3) minimizes the rank of residual errors of \mathbf{A} against the target rank, instead of the nuclear norm. A major drawback of using nuclear norm to approximate l^0 -norm of singular values is that the nuclear norm minimizes not only the rank of \mathbf{A} , but also the variance of \mathbf{A} by simultaneously minimizing all the singular values of \mathbf{A} including the singular values within the target rank N , i.e. $\sigma_{1 \leq i \leq N}$. Consequently, the low rank structure of \mathbf{A} may not be well approximated under the environment that does not follow the assumption of large number of inputs.

Although Eq. (3) is non-convex, we observe in our experiments that Eq. (3) encourages the resulting low-rank matrix to have a rank close to N even with deficient observations. For example, when the singular values of \mathbf{A} within the target rank are small, the nuclear norm can result in a rank deficient matrix \mathbf{A} , i.e. whose rank is smaller than the target rank. In contrast, because our work does not minimize the subspace variance of \mathbf{A} within the target rank, we are not biased to the solution with smaller variance of \mathbf{A} . Thus, the low rank matrix \mathbf{A} can be more accurately estimated. Further analyses and discussions about this claim are provided in this paper in later sections.

In contrast to MF methods where the a priori rank constraint is enforced as a hard constraint via matrix projection, we enforce the rank constraint as a soft constraint and propose the Partial Singular Value Thresholding (PSVT) to solve our partial sum singular value objective function. As analyzed in our study, the PSVT operator encourages the result \mathbf{A} to meet the target rank even when all the singular values are small.

This work is the extension of our previous conference paper [34]. We empirically studied the proposed objective function in many low-level vision problems, e.g. HDR imaging, photometric stereo, and image alignment, where the theoretical rank of \mathbf{A} is known and the number of observations is limited. Our experimental analyses show that our formulation, described in Eq. (3), converges to a solution more robust to outliers than the solution obtained by the objective function in Eq. (2) in rank minimization, when the number of observations is limited. Empirically, we also found that the solutions of Eq. (2) and Eq. (3) are almost identical when more than a sufficient number of samples is observed.

In short summary, our contributions are as follows:

- We present a partial sum objective function and its corresponding minimization method for RPCA.

- We empirically study the partial sum objective function and claim that it outperforms the nuclear norm rank minimization when the number of observed samples is very limited.
- We present the convergence property of the proposed algorithm to minimize the proposed partial sum objective function consisting of PSSV and sparse term, and provide its proof.
- We apply our technique on various low-level vision problems and demonstrate superior results over previous works.

2 RELATED WORKS

In this section, we briefly review early works related to RPCA, then we discuss some recent advances in RPCA and its applications in computer vision. We will also review some recent factorization (MF) based works for low-rank approximation. We invite readers to refer to Candès *et al.* [10] for a thoughtful review of RPCA.

In conventional PCA [31], the goodness-of-fit of data is evaluated by the l^2 -norm which is very sensitive to outliers. Early works in RPCA tried to reduce the effects of outliers by random sampling [21], robust M-estimator [14], [15], or alternating minimization [32] to identify outliers or to penalize data with large errors. These methods share some limitations: either they are sensitive to the choice of parameters or their algorithms are not polynomial in running time.

Recent advances in RPCA showed that the heuristic nuclear norm solution [10], [39], [43] converges to a solution which is robust to sparse outliers. Candès *et al.* [10] proved that the original RPCA problem as in Eq. (1) can be solved by instead solving the convex relaxation version in Eq. (2), and it provides a unique and *exact* solution of Eq. (1) as long as \mathbf{E} is sparse and random and the underlying rank(\mathbf{A}) is lower than a certain upper bound¹. To solve Eq. (2), various methods have been proposed [33], [44]. Among them, Alternating Direction Method of Multipliers (ADMM, or called inexact augmented Lagrange multiplier) [33] has shown to be computationally efficient. Also, Zhou *et al.* [50] and Agarwal *et al.* [1] proved that convex approximation by nuclear norm can still achieve bounded and stable results even under small noise measurements.

Besides the standard nuclear norm relaxation, there are also works that study variants of nuclear norm to enhance performance of rank minimization [12], [22], [26]. Chen *et al.* [12] and Gaiffas *et al.* [22] proposed an adaptive weighted nuclear norm. They suggested a non-trivial update scheme to update the adaptive weighted nuclear norm and claimed to achieve higher accuracy in low rank matrix approximation in comparison with the standard nuclear norm. Hu *et al.* [26] proposed the truncated nuclear norm (TNN) for the matrix completion problem which shares a similar objective function with

1. The bound depends on the matrix size.

our PSSV objective function. Since the TNN is non-convex which is not easy to directly solve, they aim to avoid direct minimization by locally approximating TNN as $\min_{X,W} \|X\|_* - \text{Tr}(A_l W B_l^\top)$, s.t. $X = W$ by alternatively minimizing A_l, B_l, X and W based on the singular value thresholding operator [9]. This alternating scheme requires outer iterations and additional SVD computation. Instead of utilizing this alternating scheme, we propose the PSVT operator to directly minimize the partial sum of singular value part. Although our objective function is also non-convex, our proposed PSVT produces the closed-form solution to the sum of PSSV term and proximity term. In that sense, every sub-problem of our problem has closed-form solution. Thus, our optimization problem can be solved efficiently and exactly. Moreover, while Hu *et al.* is dedicated only to matrix completion, we show that our work can be successfully applied for several computer vision tasks spanning from image alignment to photometric stereo and HDR imaging.

Another branch of low-rank framework is based on MF. Several robust MF methods based on l_1 -norm have been suggested [8], [20], [49]. A benefit of matrix factorization approaches is that they can easily enforce the rank constraint by the explicit bilinear matrix form. The target rank constraint is enforced as a hard constraint via matrix reprojecting or orthogonal procrustes. Cabral *et al.* [8] revisited the relationship between nuclear norm regularization and bilinear MF model [2], and proposed a rank continuation heuristic to avoid local minima. Compared with MF methods, our target rank constraint is expressed as a soft constraint which provides flexibility to balance between the target rank constraint and other constraints used in different problems.

The robustness and scalability of the rank minimization algorithm for RPCA [10], [33], [44] have inspired many applications in computer vision, such as background subtraction [10], image and video restoration [30], image alignment [38], regular texture analysis [48], and robust photometric stereo [46]. These applications are based on the observation that the underlying structures of clean data are linearly correlated, which forms a low-rank data matrix. The rank minimization proposed by Candès *et al.* [10] is general in the sense that it does not require to know a priori the rank of clean data. However, as briefly mentioned in the introduction, in some applications, the rank of clean data can be determined by the problem definition, and this motivates us to investigate how the a priori rank information can be fully utilized in the context of RPCA.

The success of rank minimization based RPCA comes from the blessing of dimensionality of input matrix [18], [43], implying large amount of observations. However, when the number of observations is limited, which is common in practice, results from RPCA might be degenerated, e.g. correct samples might be considered as outliers and vice versa. As discussed in the introduction, this happens because the standard nuclear norm

minimizes not only the rank of the matrix, but also the variance of data distribution of the matrix. To overcome the limitation, we introduce an alternative objective function that can efficiently deal with a deficient number of samples in the rank minimization problem. This work can be considered as an addendum to the standard rank minimization approach when the target rank or the approximate target rank is known. The proposed alternative objective function can control the lower bound of the rank with a simple and efficient minimizer. We demonstrate the effectiveness of our proposed objective function through thoughtful experiments.

3 PARTIAL SUM MINIMIZATION BY THE PSVT OPERATOR

3.1 Derivation of Partial Sum of Singular Values

Our partial sum formulation in Eq. (3) is originated from the following objective function:

$$\arg \min_{\mathbf{A}, \mathbf{E}} |\text{rank}(\mathbf{A}) - N| + \lambda \|\mathbf{E}\|_0, \text{ s.t. } \mathbf{O} = \mathbf{A} + \mathbf{E}. \quad (4)$$

Eq. (4) aims to recover a low-rank matrix \mathbf{A} close to the target rank N and a sparse error matrix \mathbf{E} .

Since the above objective function is also a NP-hard problem, we relax it with an alternative tractable representation. The relaxation is similar to the method presented by Candès *et al.* [10]. We should also properly interpret the target rank N . We relax it with a projection operator to enforce a rank- N matrix in a matrix interpretation manner. From the relaxation, the PSSV objective function, which is the first term in Eq. (4), can be derived as follows:

$$\begin{aligned} \|\mathbf{A}\|_* - \|P_N(\mathbf{A})\|_* &= \left| \sum_{i=1}^{\min(m,n)} \sigma_i(\mathbf{A}) - \sum_{i=1}^N \sigma_i(\mathbf{A}) \right| \\ &= \sum_{i=N+1}^{\min(m,n)} \sigma_i(\mathbf{A}) = \|\mathbf{A}\|_{p=N}, \end{aligned} \quad (5)$$

where $\|\cdot\|_{p=N}$ is denoted as the norm of PSSV with the target rank N , and $P_r(\cdot)$ is the matrix projection operator to rank r matrix defined as

Definition 1. [Projection operator]

$$P_r(\mathbf{X}) = \mathbf{U}_{1:r}^\top \mathbf{X} \mathbf{V}_{1:r}, \quad (6)$$

where $\mathbf{U}_{1:r}$ and $\mathbf{V}_{1:r}$ are the matrices consisting of the singular vectors corresponding to the r largest singular values of \mathbf{X} .

3.1.1 From rank constraint to projection

Eq. (5) leads us to the PSSV objective function in Eq. (3). In this section, we show the relationship between the target rank N and the projection operator in Eq. (5). We first introduce a rank representation.

Lemma 1. Let $\mathbf{A} \in \mathbb{R}^{m \times n}$ and $\text{rank}(\mathbf{A}) \geq r$, then there exist matrices $\mathbf{C} \in \mathbb{R}^{r \times m}$ and $\mathbf{B} \in \mathbb{R}^{n \times r}$ such that $\mathbf{C}\mathbf{C}^\top = \mathbf{B}^\top\mathbf{B} = \mathbf{I} \in \mathbb{R}^{r \times r}$ and

$$\text{rank}(\mathbf{CAB}) = r. \quad (7)$$

Proof. Let $\mathbf{U}\mathbf{D}\mathbf{V}^\top$ be SVD of \mathbf{A} . Suppose $\mathbf{C} = \mathbf{U}_{1:r}^\top$ and $\mathbf{B} = \mathbf{V}_{1:r}$, where $\mathbf{U}_{1:r}$ and $\mathbf{V}_{1:r}$ are the matrices consisting of the singular vectors corresponding to the r largest singular values. \mathbf{C} and \mathbf{B} satisfy $\text{rank}(\mathbf{CAB}) = r$, which concludes the proof. \square

The constant r can be represented in the matrix form with Lemma 1. Now, we show the characteristics of the presented solution by SVD in Lemma 1 with Lemma 2.

Lemma 2. For any $\mathbf{A} \in \mathbb{R}^{m \times n}$, $\mathbf{u} = \{\mathbf{w} | \mathbf{w} \perp \text{span}\{\mathbf{u}_1, \dots, \mathbf{u}_{k-1}\}\}$ and $\mathbf{v} = \{\mathbf{w} | \mathbf{w} \perp \text{span}\{\mathbf{v}_1, \dots, \mathbf{v}_{k-1}\}\}$,

$$\sigma_k = \max_{\mathbf{u}, \mathbf{v}} \frac{|\mathbf{u}^\top \mathbf{A} \mathbf{v}|}{\|\mathbf{u}\| \|\mathbf{v}\|}. \quad (8)$$

Lemma 2 is the well-known *Variational Characterization of Singular Values* (or *Courant-Fischer Min-max principle for singular values*). By Lemma 2, we see that \mathbf{C} and \mathbf{B} satisfying Lemma 1 are also the unique solution of the following problem:

$$\max_{\mathbf{C}, \mathbf{B}} \|\mathbf{CAB}\|_* \quad \text{s.t.} \quad \mathbf{C}\mathbf{C}^\top = \mathbf{B}^\top\mathbf{B} = \mathbf{I}. \quad (9)$$

While the solution satisfying Lemma 1 is not unique, the solution of Eq. (9) is unique. Therefore, we relax the target rank constant to the nuclear norm representation in Eq. (9) with $\mathbf{U}_{1:r}$ and $\mathbf{V}_{1:r}$ which satisfy both Lemma 1 and Eq. (9). In a summary, we show the first term in Eq. (4) can be relaxed as PSSV by Lemmas 1 and 2. This introduces the projection operator defined in Definition 1. Intuitively, when $\text{rank}(\mathbf{A}) \geq r$, as $\sigma_{i>N}(\mathbf{A}) \rightarrow 0$ (namely minimized), $\text{rank}(\mathbf{A}) \rightarrow N$. Of course, if $\text{rank}(\mathbf{O}) < N$, i.e. if the inputs are degenerated, the rank of \mathbf{A} cannot be increased to meet the target rank. This is a fundamental limitation. In common cases where input data contains noise or outliers, the inequality condition $\text{rank}(\mathbf{A}) \geq r$ is easily satisfied, because corruptions increase the rank of input data.

3.1.2 Why the partial sum of singular values?

A major advantage of using the PSSV over the nuclear norm is that it does not minimize the variance of data distribution within the target rank. Minimizing the nuclear norm can favor a solution that has a lower nuclear norm, but the singular values in residual ranks (above singular values than the target rank. Here, $N = 1$.) can be larger as illustrated in Fig. 1-(a) and Fig. 2-(a). This bias can degrade the accuracy of estimated low rank subspace. The bias phenomenon by a convex surrogate is common, and it could be corrected by non-convex relaxation [47]. An additional issue is that if the ground truth has a large variance but a sparse distribution

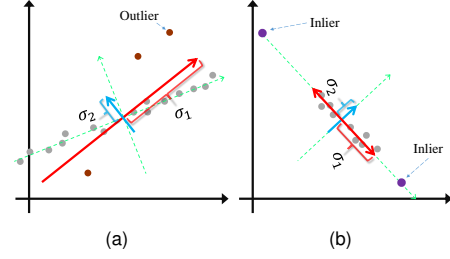


Fig. 1: Illustrations of potential problems in minimizing nuclear norm (all singular values). The ground truth subspace (Green) is a 1D line corrupted with sparse outliers and noise. In (a), the estimated subspace is biased to the estimated axis that has a smaller nuclear norm but a larger second singular value than the ground truth coordinate. In (b), some inliers located on the ground truth sub-space are regarded as outliers to achieve smaller singular value.

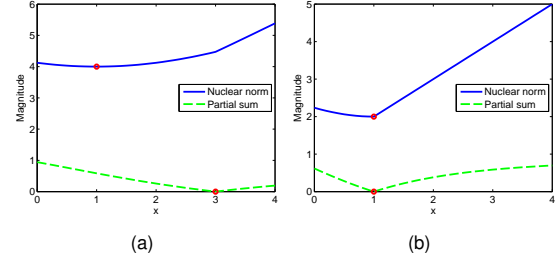


Fig. 2: A toy example comparison between the nuclear norm solution and the PSSV solution. Y-axis represents the magnitude of the nuclear norm and PSSV. The red dots represent the minimum points of the magnitude. The graphs show the nuclear norm and the PSSV of 2×2 matrices $\mathbf{A} = [1 \ 1; 3 \ x]$ in (a) and $[1 \ 1; 1 \ x]$ in (b) with x varying from 0 to 4. In (a), the minimum point of nuclear norm is at $x = 1$ where the singular values of \mathbf{A} are equal to $[3.4142, 0.5858]$ (i.e., rank-2). As for the PSSV, the minimum point is at $x = 3$ with singular values equal to $[4.4721, 0.0000]$ (i.e., rank-1). In this toy example, the nuclear norm favors a rank-2 solution over a rank-1 solution because the rank-2 solution provides the minimum nuclear norm. In contrast, the PSSV achieves the lowest rank (rank-1) solution. In (b), when the basis of the first row of \mathbf{A} is partially supported by another sample (second row), the nuclear norm and the PSSV both achieve the rank-1 solution at minima.

within the ground truth subspace, some inliers can be regarded as outliers in order to reduce the singular values within the target rank, as illustrated in Fig. 1-(b) and at the minimum point of nuclear norm in Fig. 2-(a). These two problems are not an issue when there is a lot of observed data to support the correct estimation of \mathbf{A} . However, when observed data is limited, minimizing nuclear norm can easily cause bias since there is not a sufficient number of truth samples to support large variance of \mathbf{A} within the target rank. In contrast, the PSSV does not assume small variance of \mathbf{A} , and it only minimizes variances in residual rank which corresponds to minimizing the noise variance of observed data. Note that the original rank operator, $\text{rank}(\mathbf{A})$, in Eq. (1) does not favor small variance solution.

3.2 Optimization by ADMM

Our partial sum objective function in Eq. (3) forms a constrained optimization problem. To solve this type of problems, Lin *et al.* [33] proposed an ADMM method (or called inexact augmented Lagrange multipliers, iALM). The augmented Lagrangian function of Eq. (3) is formu-

lated by:

$$L_\mu(\mathbf{A}, \mathbf{E}, \mathbf{Z}) = \|\mathbf{A}\|_{p=N} + \lambda\|\mathbf{E}\|_1 + \langle \mathbf{Z}, \mathbf{O} - \mathbf{A} - \mathbf{E} \rangle + \frac{\mu}{2} \|\mathbf{O} - \mathbf{A} - \mathbf{E}\|_F^2, \quad (10)$$

where μ is a positive scalar, and $\mathbf{Z} \in \mathbb{R}^{m \times n}$ is an estimate of the Lagrange multiplier. Directly minimizing the Lagrangian function might be particularly challenging. According to a recent development of alternating direction method [33], Eq. (10) can be solved by minimizing each variable alternatively while fixing the other variables. The optimization problem can be divided into two sub-problems:

$$\begin{aligned} \mathbf{A}^* &= \arg \min_{\mathbf{A}} L_{\mu_k}(\mathbf{A}, \mathbf{E}_k, \mathbf{Z}_k) \\ &= \arg \min_{\mathbf{A}} \mu_k^{-1} \|\mathbf{A}\|_{p=N} + \frac{1}{2} \|\mathbf{A} - (\mathbf{O} - \mathbf{E}_k + \mu_k^{-1} \mathbf{Z}_k)\|_F^2, \end{aligned} \quad (11)$$

and

$$\begin{aligned} \mathbf{E}^* &= \arg \min_{\mathbf{E}} L_{\mu_k}(\mathbf{A}_{k+1}, \mathbf{E}, \mathbf{Z}_k) \\ &= \arg \min_{\mathbf{E}} \lambda \mu_k^{-1} \|\mathbf{E}\|_1 + \frac{1}{2} \|\mathbf{E} - (\mathbf{O} - \mathbf{A}_{k+1} + \mu_k^{-1} \mathbf{Z}_k)\|_F^2, \end{aligned} \quad (12)$$

where k indicates the iteration index (see Alg. 1).

3.3 Solving \mathbf{A}^*

To minimize Eq. (11), we define the Partial Singular Value Thresholding (PSVT) operator $\mathbb{P}_{N,\tau}[\cdot]$. Before defining the PSVT, we first introduce the von Neumann's lemma (see the details in de Sá *et al.* [16]).

Lemma 3 (von Neumann [16]). *For any matrices $\mathbf{B}, \mathbf{Z} \in \mathbb{R}^{m \times n}$ and $\sigma(\cdot)$ that is a vector of the singular values, the following equality holds:*

$$\max \{ \langle \mathbf{UZV}^\top, \mathbf{B} \rangle \mid \mathbf{U} \in \mathcal{U}_m, \mathbf{V} \in \mathcal{U}_n \} = \langle \sigma(\mathbf{Z}), \sigma(\mathbf{B}) \rangle, \quad (13)$$

where \mathcal{U}_n denotes the set of $n \times n$ unitary matrices, $\langle \mathbf{A}, \mathbf{B} \rangle = \text{Tr}(\mathbf{A}^\top \mathbf{B})$ and, for any matrix $\mathbf{A} \in \mathbb{R}^{m \times n}$. Hence

$$\langle \mathbf{A}, \mathbf{B} \rangle \leq \langle \sigma(\mathbf{A}), \sigma(\mathbf{B}) \rangle. \quad (14)$$

Moreover, equality holds in Eq. (14) iff there exists a simultaneous SVD \mathbf{U} and \mathbf{V}^\top of \mathbf{A} and \mathbf{B} in the following form:

$$\mathbf{A} = \mathbf{U} \text{diag}(\sigma(\mathbf{A})) \mathbf{V}^\top \text{ and } \mathbf{B} = \mathbf{U} \text{diag}(\sigma(\mathbf{B})) \mathbf{V}^\top. \quad (15)$$

The von Neumann's lemma shows that $\langle \mathbf{A}, \mathbf{B} \rangle$ is always bounded by the inner product of $\sigma(\mathbf{A})$ and $\sigma(\mathbf{B})$. Notice that the maximum value of $\langle \mathbf{A}, \mathbf{B} \rangle$ can be only achieved when \mathbf{A} has the same singular vector matrices \mathbf{U} and \mathbf{V} as \mathbf{B} . This fact is useful to derive the PSVT.

Theorem 1 (PSVT). *Let $\tau > 0$, $l = \min(m, n)$ and $\mathbf{X}, \mathbf{Y} \in \mathbb{R}^{m \times n}$ which can be decomposed by SVD. \mathbf{Y} can be considered as the sum of two matrices, $\mathbf{Y} = \mathbf{Y}_1 + \mathbf{Y}_2 = \mathbf{U}_{Y1} \mathbf{D}_{Y1} \mathbf{V}_{Y1}^\top + \mathbf{U}_{Y2} \mathbf{D}_{Y2} \mathbf{V}_{Y2}^\top$, where $\mathbf{U}_{Y1}, \mathbf{V}_{Y1}$ are the singular vector matrices corresponding to the N largest singular*

values, and $\mathbf{U}_{Y2}, \mathbf{V}_{Y2}$ from the $(N+1)$ -th to the last from SVD, and define a minimization problem for the PSSV as

$$\arg \min_{\mathbf{X}} \frac{1}{2} \|\mathbf{X} - \mathbf{Y}\|_F^2 + \tau \|\mathbf{X}\|_{p=N}. \quad (16)$$

Then, the optimal solution of Eq. (16) can be expressed by the PSVT operator defined as:

$$\begin{aligned} \mathbb{P}_{N,\tau}[\mathbf{Y}] &= \mathbf{U}_Y (\mathbf{D}_{Y1} + \mathcal{S}_\tau[\mathbf{D}_{Y2}]) \mathbf{V}_Y^\top \\ &= \mathbf{Y}_1 + \mathbf{U}_{Y2} \mathcal{S}_\tau[\mathbf{D}_{Y2}] \mathbf{V}_{Y2}^\top, \end{aligned} \quad (17)$$

where

$$\begin{aligned} \mathbf{D}_{Y1} &= \text{diag}(\sigma_1, \dots, \sigma_N, 0, \dots, 0), \\ \mathbf{D}_{Y2} &= \text{diag}(0, \dots, 0, \sigma_{N+1}, \dots, \sigma_l), \end{aligned}$$

and $\mathcal{S}_\tau[x] = \text{sign}(x) \cdot \max(|x| - \tau, 0)$ is the soft-thresholding operator [19], [24].

Proof. Let's consider $\mathbf{X} = \mathbf{U}_X \mathbf{D}_X \mathbf{V}_X^\top = \sum_{i=1}^l \sigma_i(\mathbf{X}) u_i v_i^\top$ where $\mathbf{U}_X = [u_1, \dots, u_m] \in \mathcal{U}_m$, $\mathbf{V}_X = [v_1, \dots, v_n] \in \mathcal{U}_n$ and $\mathbf{D}_X = \text{diag}(\sigma(\mathbf{X}))$, where the singular values $\sigma(\cdot) = [\sigma_1(\cdot), \dots, \sigma_l(\cdot)] \geq 0$ are sorted in a non-increasing order. Also we define the function $J(\mathbf{X})$ as the objective function of Eq. (16). The first term of Eq. (16) can be derived as follows:

$$\begin{aligned} \frac{1}{2} \|\mathbf{X} - \mathbf{Y}\|_F^2 &= \frac{1}{2} \left(\|\mathbf{Y}\|_F^2 - 2\langle \mathbf{X}, \mathbf{Y} \rangle + \|\mathbf{X}\|_F^2 \right) \\ &= \frac{1}{2} \left(\|\mathbf{Y}\|_F^2 - 2 \sum_{i=1}^l \sigma_i(\mathbf{X}) u_i^\top \mathbf{Y} v_i + \sum_{i=1}^l \sigma_i(\mathbf{X})^2 \right) \\ &= \frac{1}{2} \|\mathbf{Y}\|_F^2 + \frac{1}{2} \sum_{i=1}^l (-2\sigma_i(\mathbf{X}) u_i^\top \mathbf{Y} v_i + \sigma_i(\mathbf{X})^2). \end{aligned} \quad (18)$$

In Eq. (18), $\|\mathbf{Y}\|_F^2$ is regarded as a constant, and thus can be ignored in the minimization of the objective function. For a more detailed representation, we change the parameterization of \mathbf{X} to $(\mathbf{U}_X, \mathbf{V}_X, \mathbf{D}_X)$ and minimize the function:

$$\begin{aligned} J(\mathbf{U}_X, \mathbf{V}_X, \mathbf{D}_X) &= \\ &= \frac{1}{2} \sum_{i=1}^l (-2\sigma_i(\mathbf{X}) u_i^\top \mathbf{Y} v_i + \sigma_i(\mathbf{X})^2) + \tau \sum_{i=N+1}^l \sigma_i(\mathbf{X}). \end{aligned} \quad (19)$$

From von Neumann's lemma, the upper bound of $u_i^\top \mathbf{Y} v_i$ is given as $\sigma_i(\mathbf{Y}) = \max \{ u_i^\top \mathbf{Y} v_i \}$ for all i when $\mathbf{U}_X = \mathbf{U}_Y$ and $\mathbf{V}_X = \mathbf{V}_Y$. The lower bound envelope of $J(\mathbf{U}_X, \mathbf{V}_X, \mathbf{D}_X)$ is obtained at $\mathbf{U}_X = \mathbf{U}_Y$ and $\mathbf{V}_X = \mathbf{V}_Y$. Then Eq. (19) becomes a function only depending on \mathbf{D}_X as follows:

$$\begin{aligned} J(\mathbf{U}_Y, \mathbf{V}_Y, \mathbf{D}_X) &= \\ &= \frac{1}{2} \sum_{i=1}^l (-2\sigma_i(\mathbf{X}) \sigma_i(\mathbf{Y}) + \sigma_i(\mathbf{X})^2) + \tau \sum_{i=N+1}^l \sigma_i(\mathbf{X}) \\ &= \frac{1}{2} \left(\sum_{i=1}^N (-2\sigma_i(\mathbf{X}) \sigma_i(\mathbf{Y}) + \sigma_i(\mathbf{X})^2) \right. \\ &\quad \left. + \sum_{i=N+1}^l (-2\sigma_i(\mathbf{X}) \sigma_i(\mathbf{Y}) + \sigma_i(\mathbf{X})^2 + 2\tau \sigma_i(\mathbf{X})) \right). \end{aligned} \quad (20)$$

Since Eq. (20) consists of simple quadratic equations for each $\sigma_i(\mathbf{X})$ independently, it is trivial to show that the minimum of Eq. (20) is obtained at $\hat{\mathbf{D}}_{\mathbf{X}} = \text{diag}(\hat{\sigma}(\mathbf{X}))$ by derivative in a feasible domain as the first-order optimality condition, where $\hat{\sigma}_i(\mathbf{X})$ is defined as

$$\hat{\sigma}_i(\mathbf{X}) = \begin{cases} \sigma_i(\mathbf{Y}), & \text{if } i < N + 1, \\ \max(\sigma_i(\mathbf{Y}) - \tau, 0), & \text{otherwise.} \end{cases} \quad (21)$$

Hence, the solution of Eq. (16) is $\mathbf{X}^* = \mathbf{U}_{\mathbf{Y}} \hat{\mathbf{D}}_{\mathbf{X}} \mathbf{V}_{\mathbf{Y}}^\top$. This result exactly corresponds to the PSVT operator where a feasible solution $\mathbf{X}^* = \mathbf{U}_{\mathbf{Y}} (\mathbf{D}_{\mathbf{Y}1} + \mathcal{S}_\tau[\mathbf{D}_{\mathbf{Y}2}]) \mathbf{V}_{\mathbf{Y}}^\top$ exists. This solution is a non-increasing operator and is the exact solution for Eq. (16). \square

Our proposed PSVT can be regarded as a special case of solving the weighted nuclear norm based objective function of Chen *et al.* [12] and Gaïffas *et al.* [22]. But we would like to notice that our method suggests how the weighted parameter (defined in their literatures) can be determined to encourage the rank constraint. Also, notice that our proposed the PSVT operator provides a closed-form solution for systems of the same form as Eq. (16) (e.g. Eq. (11)). While Eq. (11) is a non-convex function, the PSVT provides a global optimal solution for the sub-problem of \mathbf{A} (see the proof of Theorem 1).

As an analysis of PSVT, when $\tau = \infty$, the optimal solution of Eq. (16) is a low-dimensional projection of \mathbf{Y} known as singular value projection [29] which enforces the target rank constraint through projection. When $\sigma_i < \tau$ for $1 \leq i \leq N$, conventional SVT [9] projects these σ_i to zero resulting in a more deficient rank of \mathbf{A} than the target rank while our PSVT does not lead to rank deficient matrices. Hence, PSVT implicitly encourages the resulting matrix \mathbf{A} to meet the target rank even when all the σ_i are small, which occasionally happens when the number of observed samples is limited.

3.4 Solving \mathbf{E}^*

As suggested by Hale *et al.* [24], the solution to the sub-problem in Eq. (12) can be solved as:

$$\mathcal{S}_\tau[\mathbf{Y}] = \arg \min_{\mathbf{X}} \frac{1}{2} \|\mathbf{X} - \mathbf{Y}\|_F^2 + \tau \|\mathbf{X}\|_1, \quad (22)$$

where $\mathcal{S}_\tau[x] = \text{sign}(x) \max(|x| - \tau, 0)$ is the soft-thresholding operator [19], [24], and $x \in \mathbb{R}$. This operator can be extended to vectors and matrices by applying it element-wisely. The soft-thresholding (shrinkage) method is shown to be very effective in minimizing l^1 -norm and the proximity term, and guarantee that the solution is the global minimum for the same form as Eq. (22) (e.g. Eq. (12)) [19], [24].

3.5 Updating \mathbf{A}^* and \mathbf{E}^*

At each iteration, \mathbf{A}_k and \mathbf{E}_k can be updated with the operators $\mathcal{S}_\tau[\cdot]$ and $\mathbb{P}_{N, \mu_k^{-1}[\cdot]}$ as:

$$\begin{aligned} \mathbf{A}_{k+1} &= \mathbb{P}_{N, \mu_k^{-1}}[\mathbf{O} - \mathbf{E}_k + \mu_k^{-1} \mathbf{Z}_k], \\ \mathbf{E}_{k+1} &= \mathcal{S}_{\lambda \mu_k^{-1}}[\mathbf{O} - \mathbf{A}_{k+1} + \mu_k^{-1} \mathbf{Z}_k]. \end{aligned} \quad (23)$$

The iterations are terminated when the equality constraint is satisfied (in all the experiments, $\frac{\|\mathbf{O} - \mathbf{A} - \mathbf{E}\|_F}{\|\mathbf{O}\|_F} < 1e^{-7}$). Experiments showed that updating \mathbf{A}_k and \mathbf{E}_k for only one iteration in the inner loop is sufficient to produce a satisfying accurate solution of Eq. (3). This method is called the inexact ALM [33] which is designed for computational efficiency.

We summarize the overall algorithm in Alg. 1 (For more details, refer to the report of Lin *et al.* [33]).

Algorithm 1 ADMM for the PSSV based RPCA

Input : $\mathbf{O} \in \mathbb{R}^{m \times n}$, $\lambda > 0$, the constraint rank N .
Initialize $\mathbf{A}_0 = \mathbf{E}_0 = \mathbf{0}$, \mathbf{Z} as suggested in [33], $\mu_0 > 0$, $\rho > 1$ and $k = 0$.
// Outer loop
while not converged **do**
// Inner loop
while not converged **do**
 $\mathbf{A}_{k+1} = \mathbb{P}_{N, \mu_k^{-1}}[\mathbf{O} - \mathbf{E}_k + \mu_k^{-1} \mathbf{Z}_k]$.
 $\mathbf{E}_{k+1} = \mathcal{S}_{\lambda \mu_k^{-1}}[\mathbf{O} - \mathbf{A}_{k+1} + \mu_k^{-1} \mathbf{Z}_k]$.
end while
 $\mathbf{Z}_{k+1} = \mathbf{Z}_k + \mu_k (\mathbf{O} - \mathbf{A}_{k+1} - \mathbf{E}_{k+1})$.
 $\mu_{k+1} = \rho \mu_k$.
 $k = k + 1$.
end while
Output : $(\mathbf{A}_k, \mathbf{E}_k)$.

3.6 Convergence Analysis

To the best of authors' knowledge, the general convergence property of ADMM which alternates between non-convex (solving \mathbf{A}^*) and convex (solving \mathbf{E}^*) functions has not been answered yet. The ADMM for non-convex problems can be considered as a local optimization method, of which it aims to converge to a point with *better objective value* [5].

In our problem, each sub-problem has a closed-form solution and the objective value is always decreasing with respect to the optimizing parameters in each sub-problem iteration. Our empirical convergence tests showed that our ADMM based algorithm has strong convergence behavior. Although the global optimal solution is not guaranteed, all of our experiments showed that our algorithm converges to a solution which is very close to the nuclear norm solution, when the number of observations is more than sufficient. It also converges to a better solution than the nuclear norm solution when the number of observations is limited, even with all zero initializations.

Besides the empirical behavior, we provide the convergence property for Alg. 1 in Proposition 1. It shows that any accumulation point (limit point) generated along the iterations satisfies the first-order necessary optimal condition, a KKT (Karush-Kuhn-Tucker) point.

Proposition 1 (Convergence). *Let $S_k = (\mathbf{A}_k, \mathbf{E}_k, \mathbf{Y}_k, \hat{\mathbf{Y}}_k)$, where $\hat{\mathbf{Y}}_{k+1} = \mathbf{Y}_k + \mu_k (\mathbf{O} - \mathbf{A}_{k+1} - \mathbf{E}_k)$ and $\{S_k\}_{k=1}^\infty$ is a set of intermediate solutions of Alg. 1. Suppose that $\{\mathbf{Y}_k\}_{k=1}^\infty, \{\hat{\mathbf{Y}}_k\}_{k=1}^\infty$ are bounded, $\lim_{k \rightarrow \infty} (\mathbf{Y}_{k+1} - \mathbf{Y}_k) = 0$, and μ_k is non-decreasing, then any accumulation point of $\{S_k\}_{k=1}^\infty$ satisfies the following KKT conditions: (C1) $\mathbf{Y}^* \in$*

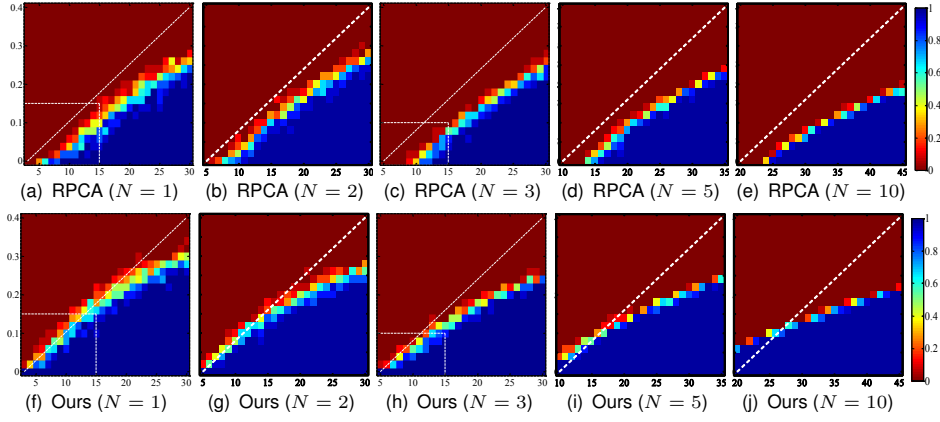


Fig. 3: Success ratio for synthetic data with varying the number of columns (observations) n . Comparison between RPCA (nuclear norm) and ours (PSSV) for rank-1,2,3,5,10 cases. X-axis represents the column size, and Y-axis represents the corruption ratio $r \in [0, 0.4]$. Color magnitude represents success ratio $[0, 1]$. The white dotted lines are provided as a guide for easier comparison.

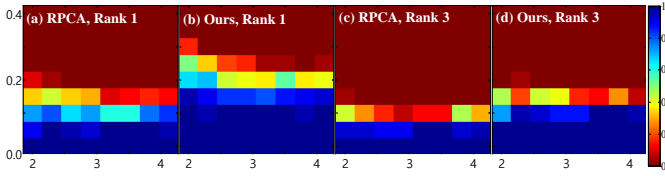


Fig. 4: Success ratio for synthetic data with varying the number of rows (dimension) m (a-d). Comparison between RPCA (nuclear norm) and ours for the rank-1 case (a,b), and for the rank-3 case (c,d). The Y-axis represents the corruption ratio $r \in [0, 0.4]$. The X-axis represents the log scale row size $\log_{10} m \in [\log_{10} 100, \log_{10} 12800]$ in (a-d). The color magnitude represents the success ratio $[0, 1]$.

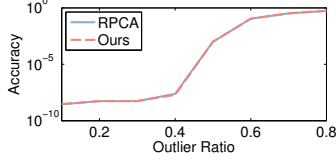


Fig. 5: Comparison on a sufficient sample condition with a rank-3 matrix $\mathbf{O} \in \mathbb{R}^{10000 \times 3000}$. Under the sufficient sample case, the nuclear norm and PSSV solutions are very similar.

$\partial^C \|\mathbf{A}^*\|_p$, (C2) $\mathbf{Y}^* \in \partial \|\lambda \mathbf{E}^*\|_1$, (C3) $\mathbf{O} - \mathbf{A}^* - \mathbf{E}^* = \mathbf{0}$, (C4) $\partial^C \|\mathbf{A}^*\|_p \cap \partial \|\lambda \mathbf{E}^*\|_1 \neq \emptyset$. In particular, whenever $\{\mathcal{S}_k\}_{k=1}^\infty$ converges, it converges to a KKT point of Eq. (3).

The proofs can be found in the supplementary material. The conditions for non-decreasing μ_k and the boundness of the sequence are already satisfied by Alg. 1 (see Lemma 1 in Lin *et al.* [33]). Proposition 1 is established for a single iteration algorithm in the inner loop, i.e. iALM. When the inner loop iterates until convergence, the proof of the above result becomes easier. We remain further theoretical analyses of convergence as future work.

4 EXPERIMENT RESULTS

We compare the performance of the proposed method against RPCA (nuclear norm) [10] with synthetic data sets and real world application examples. In all the experiments, we use the default parameters recommended by Candès *et al.* [10] for both their approach and ours, i.e. $\lambda = 1/\sqrt{\max(m, n)}$ and $\rho = 1.5$, except if explicitly stated otherwise.

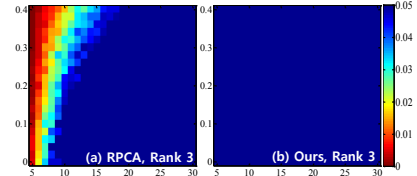


Fig. 6: Comparison for the rank deficiency of the estimated low-rank matrix $\hat{\mathbf{A}}$ for the rank-3 case, obtained by RPCA (a) and our method (b). The red regions indicate rank deficiency, i.e. the rank of the recovered matrix is lower than the constraint rank. X-axis represents the column size, and Y-axis represents the corruption ratio $r \in [0, 0.4]$. Color magnitude represents success ratio $[0, 1]$.

4.1 Synthetic Dataset

We compare our method (PSSV) with RPCA (nuclear norm) on synthetic data by evaluating the success ratio and convergence behaviors. To synthesize a ground-truth low-rank matrix $\mathbf{A}_{GT} \in \mathbb{R}^{m \times n}$ of rank N , we perform a linear combination of N arbitrary orthogonal basis vector. The weight vector used to span each column vector of \mathbf{A}_{GT} is randomly sampled from the uniform distribution $U[0, 1]$. To generate sparse outliers, we select $m \times n \times r$ entries from \mathbf{A}_{GT} , where r denotes the corruption ratio. Larger r means more outlier entries. The selected entries are corrupted by random noise from $U[0, 1]$. We ran each of the tests over 50 trials and report the average errors of the overall trials. We refer $\frac{\|\mathbf{A}_{GT} - \hat{\mathbf{A}}\|_F}{\|\mathbf{A}_{GT}\|_F}$ as normalized MSE.

4.1.1 Comparison of Success Ratio

We verify the robustness of RPCA (nuclear norm) and the proposed method (PSSV) with respect to the number of observations, data dimension and the corruption ratio from \mathbf{E} . We examine the performance by counting the number of successes. If the recovered $\hat{\mathbf{A}}$ has a normalized MSE smaller than 0.01, we consider the estimation of \mathbf{A} and \mathbf{E} is successful. We compare the success ratio with varying the column size n (i.e. the number of observations), and the row size m (i.e. data dimension). The magnitude in Fig. 3 indicates the percentage of success. A larger blue area indicates a more robust performance of the algorithm.

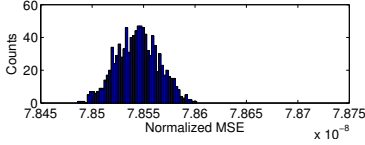


Fig. 7: Distribution of residual errors with 1000 different random initializations.

We have also performed experiments where we fixed $m = 10,000$ and varied n and r . The comparison between RPCA and our method with rank-1,2,3,5 and -10 constraint is shown in Fig. 3. As n decreases (i.e. the number of observations decreases), the success ratio of RPCA decreases more rapidly than our method. When more observations are available (over $n = 25$ in Fig. 3 and Fig. 5), both methods show a similar behavior.

Fig. 4 shows the success ratio of RPCA and ours for the varying row m cases. We fixed $n = 16$, and varied m and r . Our method can successfully recover \mathbf{A} and \mathbf{E} with input data contaminated up to 15% of severe corruption for the rank-1 case in Fig. 4-(b), and leads to more robust results than RPCA despite 5% higher corruption for the rank-3 case in Fig. 4-(d).

4.1.2 Rank Deficiency

We verify whether the recovered $\hat{\mathbf{A}}$ obtained by RPCA and our method is rank deficient. Our objective function minimizes rank up to the target rank. Thus, the result rank of $\hat{\mathbf{A}}$ should not be lower than the target rank. In practice, rank deficiency is crucial for quality of the final solution in some applications (e.g. photometric stereo). We measure the ratio $\sigma_N(\hat{\mathbf{A}})/\sigma_1(\hat{\mathbf{A}})$ (similar to the inverse value of the condition number) for the rank- N constraint case. We only test for rank- $N = 3$ as a typical example of photometric stereo. If the ratio is lower than 0.01, we consider that the recovered matrix has a rank lower than N . In Fig. 6, the red regions mean that the rank of the recovered matrix is lower than the target rank. The experiments empirically validate that the rank obtained by our method is bounded for almost all of the regions, while RPCA has regions whose rank is lower than the target rank. This happens when observations do not support its true subspaces well.

4.1.3 Sensitivity to Initialization

Since the proposed objective function is non-convex, the converged solution may be different according to initialization. To study the sensitivity of the optimization, we conducted 1000 experiments with random initialization on a rank-3 matrix $\mathbf{O} \in \mathbb{R}^{10000 \times 50}$ with 5% outliers. The distribution of normalized MSE is shown in Fig. 7. While the convergence of non-convex problem to a local optimum is hard to be guaranteed, most solutions are concentrically distributed in regions near the ground-truth solution with small errors.

4.1.4 Comparisons with other low-rank approximations

We provide additional comparisons with the singular value projection (SVP) [29] based and the weighted

Method	Objective function
Eriksson <i>et al.</i> [20]	$\min_{\mathbf{U}, \mathbf{V}} \ \mathbf{O} - \mathbf{UV}\ _1$
Zheng <i>et al.</i> [49]	$\min_{\mathbf{U}, \mathbf{V}} \ \mathbf{O} - \mathbf{UV}\ _1 + \lambda \ \mathbf{V}\ _{w,*}$ s.t. $\mathbf{U}^T \mathbf{U} = \mathbf{I}$
LMaFit [40]	$\min_{\mathbf{A}, \mathbf{U}, \mathbf{V}} \ \mathbf{O} - \mathbf{A}\ _1$ s.t. $\mathbf{A} = \mathbf{UV}$
SVP [29] based RPCA	$\min_{\mathbf{A}, \mathbf{E}} \ \mathbf{E}\ _1$ s.t. $\mathbf{O} = \mathbf{A} + \mathbf{E}, \text{rank}(\mathbf{A}) = N$
RPCA [10]	$\min_{\mathbf{A}, \mathbf{E}} \ \mathbf{A}\ _{w,*} + \lambda \ \mathbf{E}\ _1$ s.t. $\mathbf{O} = \mathbf{A} + \mathbf{E}$
WNNM [12] based RPCA	$\min_{\mathbf{A}, \mathbf{E}} \ \mathbf{A}\ _{w,*} + \lambda \ \mathbf{E}\ _1$ s.t. $\mathbf{O} = \mathbf{A} + \mathbf{E}$
Our method	$\min_{\mathbf{A}, \mathbf{E}} \ \mathbf{A}\ _{p=N} + \lambda \ \mathbf{E}\ _1$ s.t. $\mathbf{O} = \mathbf{A} + \mathbf{E}$

TABLE 1: Summary of the compared methods. $\mathbf{O}, \mathbf{A}, \mathbf{E} \in \mathbb{R}^{m \times n}$, $\mathbf{U} \in \mathbb{R}^{m \times N}$, $\mathbf{V} \in \mathbb{R}^{N \times n}$, $\|\cdot\|_{w,*}$ is the weighted nuclear norm and the weight coefficients in w is determined adaptively as suggested by Chen *et al.* [12].

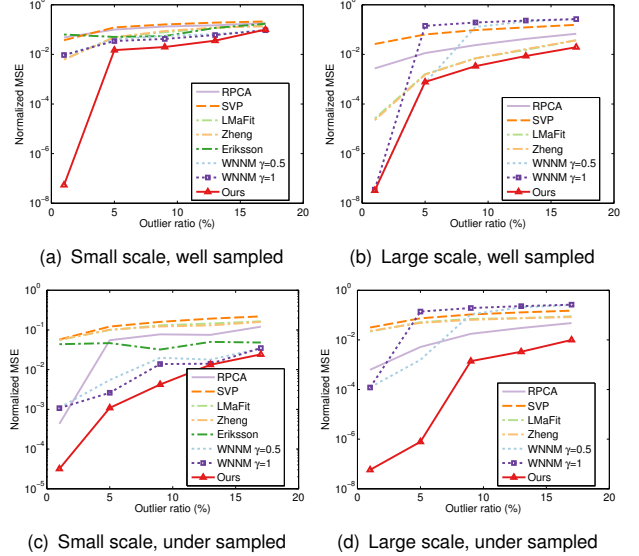


Fig. 8: Accuracy comparisons with varying outlier ratio and deficient number of samples for SVP [29] based and WNNM [12] based methods, LMaFit [40], Zheng *et al.* [49], Eriksson *et al.* [20], and our method. The experiments consist of small scale problems ($\mathbf{O} \in \mathbb{R}^{30 \times 7}$ with rank-2) in (a,c) and large scale problems ($\mathbf{O} \in \mathbb{R}^{5000 \times 20}$ with rank-3) in (b,d). The cases with well-sampled data and under-sampled data on subspaces are shown at the top and bottom rows respectively. X-axis represents the percentage of outlier, and Y-axis represents the average error. LMaFit, Zheng *et al.* and Eriksson *et al.* are MF methods. MF methods also result in low accuracy under the case of deficient number of samples. Comparing (b) and (d), MF methods are prone to the data under-sampled on subspaces, because bilinear model enforcedly constrains the target rank and excessively attempts to match it.

nuclear norm (WNNM) [12] based methods, and low-rank matrix approximation approaches by MF. The formulations are summarized in Table 1. The SVP and WNNM are reformulated based on RPCA framework for fair comparison. MF methods enforce the target rank N constraint of data matrix ($\mathbf{O} = \mathbf{UV}$) by factorizing it into a product of rank- N basis (\mathbf{U}) and coefficient (\mathbf{V}) as hard constraint. Among the existing MF based methods, we compare with the state-of-the-art methods of LMaFit [40], Zheng *et al.* [49] and Eriksson *et al.* [20], with the default recommended parameters.

Since the method of Eriksson *et al.* can only handle toy size examples, we perform separate experiments for small and large scales. We synthetically generate the data matrix $\mathbb{R}^{30 \times 7}$ with rank-2 for small scale or $\mathbb{R}^{5000 \times 20}$ with rank-3 for large scale, and varying corruption ratio on [0.05, 0.20]. Normalized MSE is displayed in Fig. 8-(a,b).

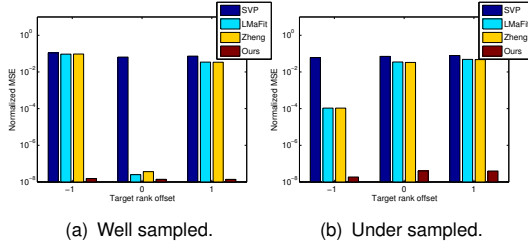


Fig. 9: Effects when the target rank is incorrectly set. We set the input target rank $N = N_{\text{true}} + t_{\text{offset}}$, where the truth rank $N_{\text{true}} = 3$. The lower value the better.

Compared to our method, their approach also minimizes the nuclear-norm in addition to the hard target rank constraint. As discussed previously, since minimizing the nuclear-norm also implicitly minimizes the variance of estimated low rank matrix, their estimated low rank matrix could be biased by this assumption. On the other hand, since our PSSV objective function does not have this assumption, and since the target rank is enforced softly, our method converges to more accurate solutions compared to the solutions of LMaFit, Zheng *et al.* and Eriksson *et al.*

We have also conducted experiments for the under-sampled cases on subspace: e.g. a ground truth data is spanned with 3 basis axis (true and target rank are 3), but the distribution along the third basis axis has a very small variance (small singular value). Thus, although the underlying matrix is a rank-3 matrix, it is very close to a rank-2 matrix. This situation often happens when the last basis is less supported by a few true samples. This is also called the unbalanced singular values case (e.g. $\sigma(\mathbf{A}) = [100, 10, 1e^{-1}]$). Our results shown in Fig. 8-(c,d) have smaller errors than results from LMaFit, Zheng *et al.* and Eriksson *et al.* even for the under-sampled cases.

4.1.5 Incorrect Setting of Target Rank

Our method requires the target rank as an input parameter. When the target rank is set incorrectly, the question of the behavior of our method naturally arises. For the sake of completeness, we have experimented with incorrect target rank setting in Fig. 9.

We considered the situation that the rank is known, but ambiguous within some bound (e.g., the truth rank is 3, but ambiguous within rank- $\{2,3,4\}$). The data construction is similar to the experiments conducted in Sec. 4.1.4, i.e. well-sample and under-sampled data cases. The rank-3 matrices $\mathbf{O} \in \mathbb{R}^{3000 \times 100}$ are used for experiment. Fig. 9 shows that MF based methods are prone to incorrect target rank setting. Interestingly, for the data under-sampled on subspaces, MF based methods with a target rank lower than the true rank show better performance than well-sampled data case. This is because the bilinear model enforcedly constrained the target rank within the bilinear matrix structure. Therefore, when the 3rd basis is weakly supported by samples, fitting with rank-2 bilinear model only for the 1st and 2nd basis provides better precision than using rank-3 bilinear model. This result is consistent with Fig. 8-(b,d).

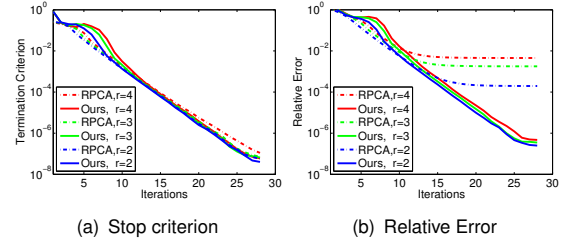


Fig. 10: Convergence behavior of RPCA [33] and our method for the rank 2,3 and 4.

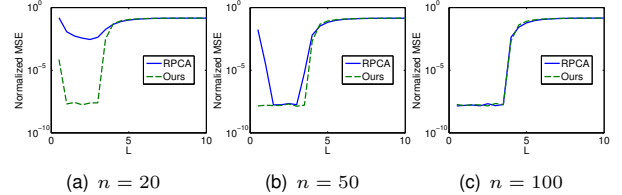


Fig. 11: Evolution of the normalized MSE according to varying $\lambda = L/\sqrt{\min(m, n)}$. For experiments, rank-3 matrices $\mathbf{O} \in \mathbb{R}^{5000 \times n}$ are generated with 5% outliers.

4.1.6 Convergence Behavior

To examine the convergence behavior of both RPCA [33] and our method, we plot the evolution of the relative errors $\frac{\|\mathbf{A}_{GT} - \hat{\mathbf{A}}\|_F}{\|\mathbf{A}_{GT}\|_F} + \frac{\|\mathbf{E}_{GT} - \hat{\mathbf{E}}\|_F}{\|\mathbf{E}_{GT}\|_F}$ and termination criteria $\frac{\|\mathbf{O} - \mathbf{A} - \mathbf{E}\|_F}{\|\mathbf{O}\|_F}$ over the iterations in Fig. 10-(a) and (b), respectively. We randomly generated 5000×40 matrices for the rank-2, 3, 4 cases, and the average value over the trials is computed.

We use the *MATLAB* implementation of RPCA provided by Wright *et al.* [44], and our method is terminated at similar moments with RPCA as shown in Fig. 10-(a). Thus, the execution time of our algorithm is the same as with inexact ALM based RPCA [33]. Fig. 10-(b) also shows that our method provides higher accuracy than RPCA as well as a gradual convergence under the same termination criterion.

4.1.7 Lambda (λ) parameter

We conduct all the experiments in this paper with the same λ parameter recommended by Candès *et al.* [10]. For completeness, we show in this section how the choice of λ can affect the solution of both RPCA and ours. Note that tuning the optimal λ to balance the nuclear norm and sparsity is not possible unless the ground truth solution is known as discussed by Chandrasekaran *et al.* [11]. Thus, the results provided in here are only for reference. Fig. 11 shows normalized MSE when λ varies, where $\lambda = L/\sqrt{\max(m, n)}$. The results show that our method consistently produces less errors than RPCA under different settings of λ .

4.2 Real-world Applications

4.2.1 High Dynamic Range (HDR) Imaging

We apply the proposed method for modeling a background scene and a ghost-free HDR composition. The input is a set of low dynamic images and the goal is to composite an HDR image using RPCA to reject

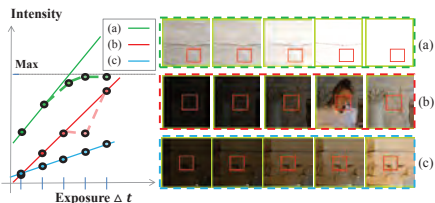


Fig. 12: Illustration of the observed intensity values for (a) saturation region, (b) moving object, and (c) consistent cases. Solid lines denote ideal relationship between intensity and exposure, and dots and dotted lines denote the observed intensities.

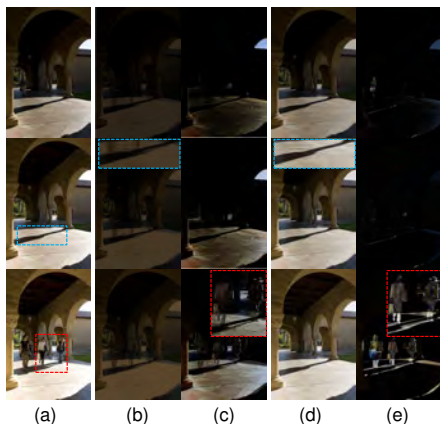


Fig. 13: Comparison of the low-rank matrix and sparse error results between RPCA and ours on the *Arch* dataset [23]. (a) Three out of the five input multi-exposure image samples. Low-rank (b,d) and sparse error (c,e) results, respectively obtained by RPCA (b,c) and the proposed approach (d,e).

outliers, such as moving objects and saturations, in the Low Dynamic Range (LDR) images. We assume that the differently exposed images I_i are aligned and the camera response function (CRF) is calibrated (or linear). Then, the captured images can be represented as $I_i = \kappa R \Delta t_i$, where R denotes the sensor irradiance, Δt_i is the exposure time for the i -th image, and κ is a positive scalar. We construct the observed intensity matrix $\mathbf{O} \in \mathbb{R}^{m \times n} = [\text{vec}(I_1) \cdots \text{vec}(I_n)]$ by stacking the vectorized input images, where m and n are the number of pixels and images respectively. Since the intensities of input images are linearly dependent, the ideal solution of this problem is rank-1. However, in practice, $\text{rank}(\mathbf{O})$ is higher than 1 due to moving objects, saturation or other artifacts (illustrated in Fig. 12). We apply RPCA (nuclear norm) and our method (PSSV) to each color channel independently, in order to separate artifacts and background scene.

The *Arch* and *Sculpture Garden* datasets from Gallo *et al.* [23] are used for evaluation. The estimated backgrounds as low-rank matrix and the sparse outliers from the RPCA and our method are shown in Fig. 13. The example in Fig. 13-(a) consists of only 5 input images which is very limited. Ideally, the decomposed low-rank matrix $\mathbf{A} = [\text{vec}(A_1) \cdots \text{vec}(A_n)]$ consists of relative intensities of the background scene from which moving objects or saturation artifacts should be removed (see Fig. 13-(b,d)). RPCA returns a low-rank matrix whose magnitude differs drastically from the input image, as

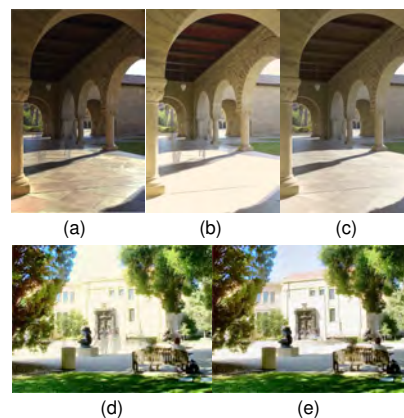


Fig. 14: HDR composition results for the Arch (top) and Sculpture Garden (bottom) datasets by Gallo *et al.* [23]. (a) Debevec *et al.* [17]. (b,d) RPCA. (c,e) the proposed method.

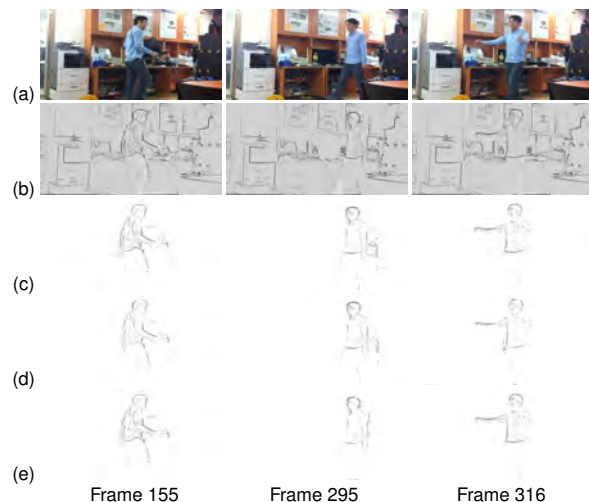


Fig. 15: Motion detection comparison between RPCA and our method on a varying illumination dataset. (a) Representative sampled inputs. (b-c): Results of RPCA, with $n = 5$ and 100 respectively. (d-e): Our results, with $n = 5$ and 100 respectively.

shown in Fig. 13-(b). Moreover RPCA yields a dense non-zero entries in \mathbf{E} , instead of being sparse, as shown in Fig. 13-(c). This situation is similar to the example in Fig. 2 where the minimum nuclear norm favors a solution with smaller variance of magnitudes. In contrast, our proposed method shows a correctly modeled background scene and successfully detects outlier regions, as shown in Fig. 13-(d,e). For displaying the sparse components in Fig. 13-(c,e), each color component (R,G,B) is set with $(|\mathbf{E}_R|, |\mathbf{E}_G|, |\mathbf{E}_B|)$, where $\mathbf{E}_{\{R,G,B\}}$ denotes sparse error matrix for each channel.

After we estimate the low-rank matrix, we composite the HDR images using the standard method of Debevec *et al.* [17]. The final HDR results are shown in Fig. 14. Because the background modelling by RPCA is inaccurate, ghosting appears in their HDR results. In contrast, our results are ghost-free.

4.2.2 Motion Detection by Temporal Edge

RPCA-based background modeling for surveillance purpose requires a large number of observations to estimate background and moving objects under global illumi-

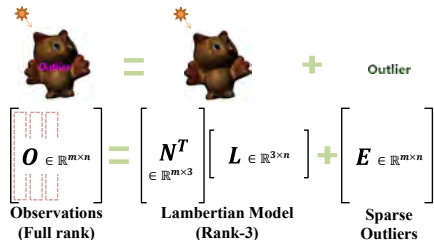


Fig. 16: Photometric stereo illustration for the used model.

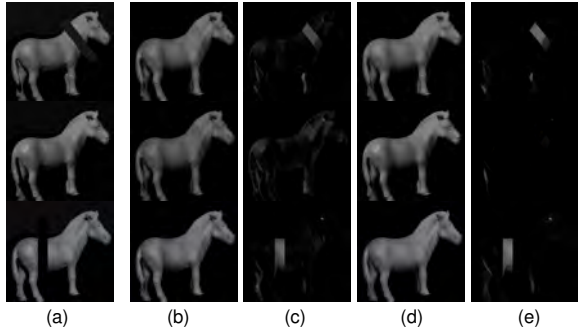


Fig. 17: Outlier rejection results for Photometric Stereo. (a) Three sampled input images out of five. (b-c) low-rank and sparse image from Wu *et al.* [46]. (d-e) low-rank and sparse image from ours.

nation changes. Such requirement is not suitable for online algorithm in surveillance. Using a few images as input, the moving region detection by RPCA could fail due to limited number of observations. In this problem, we observe that edge images make moving object boundaries more sparse and they rarely overlapped. We stack a few n edge images (obtained by Sobel operator) in video sequence as column vectors of a matrix $\mathbf{O} \in \mathbb{R}^{m \times n} = [\text{vec}(O_1) \cdots \text{vec}(O_n)]$. Without moving objects, the edge pixels on the background texture are static. So the matrix \mathbf{O} should be low-rank, essentially, rank-1. Since moving object regions are not consistent with background edges, the regions can be modeled as sparse outliers.

Fig. 15 shows the comparisons with RPCA and the proposed method. RPCA fails to decompose low-rank and sparse matrix in Fig. 15-(b) due to deficient observations where $n = 5$. On the other hand, our method successfully estimates moving object boundary, and the results are similar to the one obtained with many observations in Fig. 15-(e).

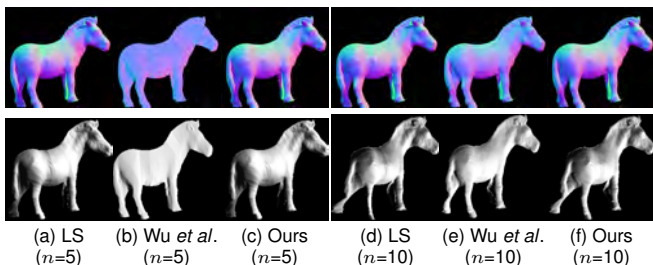


Fig. 18: Results of the photometric normal estimation and depth by LS method [42], Wu *et al.* [46] and ours. Top row: the normal estimation. Bottom row: the reconstructed depth from the estimated normals. n denotes the number of input images.

	σ_1	σ_2	σ_3	σ_4	σ_5
Input $\sigma_i(O_G)$	137.88	23.59	19.55	15.56	12.99
RPCA $\sigma_i(\mathbf{A}_G)$ in Fig. 18-(b)	125.71	7.26	0.0001	0.00	0.00
Ours $\sigma_i(\mathbf{A}_G)$ in Fig. 18-(c)	139.16	23.01	16.33	1.59	0.15

TABLE 2: Singular values of photometric stereo input for $n = 5$ in Fig. 17 and Fig. 18-(b,c).

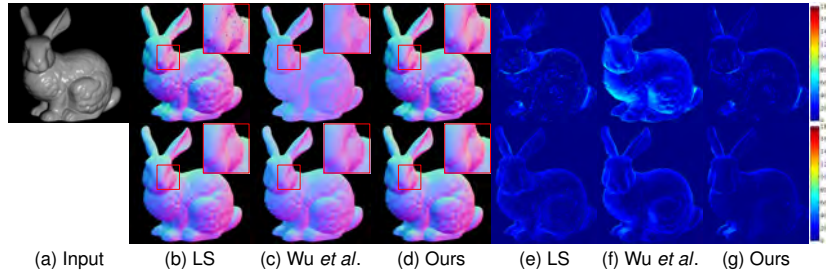
4.2.3 Outlier Rejection for Photometric Stereo

In the Lambertian model photometric stereo, $\mathbf{O} = [\text{vec}(O_1) \cdots \text{vec}(O_n)] = \mathbf{N}^T \mathbf{L}$, where $\mathbf{O} \in \mathbb{R}^{m \times n}$, $\mathbf{N} \in \mathbb{R}^{3 \times m}$ and $\mathbf{L} \in \mathbb{R}^{3 \times n}$ denote measured intensity, normal and light direction matrix, respectively, and m and n are the number of pixels and images. Hayakawa *et al.* [25] show that the intensity matrix lies in a subspace of rank 3, as illustrated in Fig. 16. However, this constraint is hardly satisfied in real situations due to shadow from self-occlusion, saturation and some object materials which do not exactly follow the Lambertian diffusion model. Considering the rank-3 constraint, the artifacts mentioned above can be regarded as sparse outliers and we get a low-rank structure as $\mathbf{O} = \mathbf{N}^T \mathbf{L} + \mathbf{E}$.

The robust photometric stereo with outlier rejection can be formulated into a RPCA problem as suggested by Wu *et al.* [46]. We compare our method with the standard least square (LS) method [42] and RPCA by Wu *et al.* [46]. The LS based photometric stereo estimates the normals by minimizing $\|\mathbf{O} - \mathbf{N}^T \mathbf{L}\|_F^2$. We corrupt some input images by painted artifacts to mimic outliers. The corrupted inputs are included in 2 out of $n = 5$ inputs (Fig. 17 and Fig. 18-(Top)), and 4 out of $n = 10$ inputs (Fig. 18-(Bottom)). Outlier rejection results are shown in Fig. 17. We present qualitative comparison of normal recovery results in Fig. 17 and Fig. 18. Wu *et al.* return a planar surface normal when the rank of input matrix is lower than 3 due to the lack of observations (italic in Table 2). When more input images are available, RPCA begins to return detail preserved results, as shown in Fig. 18-(e). On the other hand, our method consistently provides robust results for both limited and sufficient observations, as shown in Fig. 18-(c,f).

For quantitative results, we use the *Bunny* dataset [28] generated using the Cook-Torrance reflectance model and consisting of 40 different lighting conditions. The average ratio of specular and shadow regions in *Bunny* are 8.4% and 24% respectively, which act as outliers. Table 3 shows quantitative results. We vary the number of images and add 5% of uniformly distributed corruption. Each value in Table 3 is averaged over 20 randomly selected test sets. Wu *et al.* [46] produce degenerated results, as the rank of the resulting matrix is lower than 3 due to the lack of supports from the observations. When more input images are available, RPCA returns more satisfying results, but still the accuracy is lower than LS method. In contrast, our method provides robust results for both limited and sufficient observations.

No. Image	Mean error (in degrees)			Max error (in degrees)			Standard deviation		
	LS	[46]	Ours	LS	[46]	Ours	LS	[46]	Ours
5	8.53	27.88	7.06	159.72	130.77	120.78	14.48	16.45	12.30
8	9.03	13.34	5.87	142.45	139.07	85.48	11.24	10.96	9.62
10	9.24	11.14	5.70	148.05	110.12	79.54	9.91	9.77	8.06
12	8.96	9.95	5.09	130.04	80.21	76.86	9.17	9.02	7.59

TABLE 3: Photometric stereo results of *Bunny* with 5% corruption ratio, additional specular and shadow.Fig. 19: Photometric stereo results from 5 (top) and 12 (bottom) images of *Bunny* dataset with corruption. (a) A representative input image. (b-d) Recovered surface normal by LS, Wu *et al.* [46] and ours. (e-g) Corresponding error maps for each algorithm.

4.2.4 Batch Image Alignment

Given several images of an object of interest (e.g. face), the batch image alignment task aims to align them to a fixed canonical template [7], [38]. In this problem, we search for a transformation g_i for each image I_i to make the images linearly correlated. We note \mathbf{g} the set of transformations: $\mathbf{g} = \{g_1, \dots, g_n\}$ where n is the number of images and write $\mathbf{O} \circ \mathbf{g} = [\text{vec}(I_1 \circ g_1) \cdots \text{vec}(I_n \circ g_n)]$. Contrary to the formulation of Peng *et al.* [38], we consider PSSV mathematically formulated as follows:

$$\arg \min_{\mathbf{A}, \mathbf{E}, \mathbf{g}} \|\mathbf{A}\|_{p=N} + \lambda \|\mathbf{E}\|_1, \text{ s.t. } \mathbf{O} \circ \mathbf{g} = \mathbf{A} + \mathbf{E}. \quad (24)$$

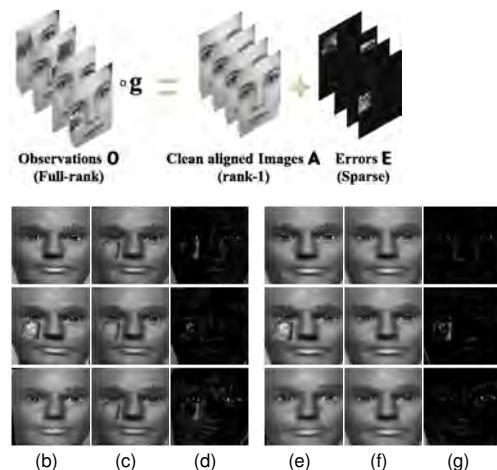
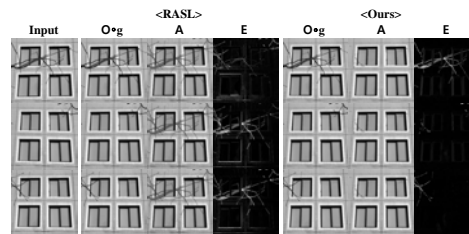
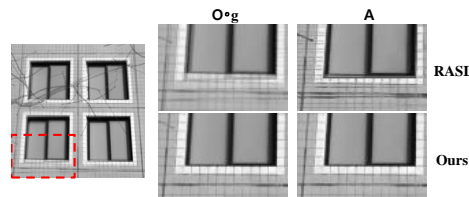
We applied our approach to the head dataset acquired under varying pose (see Fig 20-(a)) [38]. For linearly correlated noise-free batch images, the rank is $N = 1$, when the transformations for exact image alignment are estimated. Our results of alignment, low-rank estimation and error sparsity are shown in Fig 20-(e,f,g). Compared to the results obtained by RASL [38], our method can correctly detect the outliers (Fig 20-(c) v.s. Fig 20-(f)), even with only 3 input images.

Our method can correctly detect the outliers as well as robustly align the images even if the geometric model has more degrees of freedom than an affine homography model. Detailed comparisons in Fig. 22 show the average image obtained from the aligned image stack by each method. If well aligned, the average image should show seamless image without duplicated edges. Our results show fine average images due to more accurate homography estimation than RASL.

4.2.5 Image Recovery

Images of natural scenes follow natural statistics [27]. As shown in Hu *et al.* [26], information of image scenes are dominated by top 20 singular values, which is low-rank. Hu *et al.* [26] proposed a matrix completion method with the truncated nuclear norm (TNN) as introduced in Sec. 2. We formulate the matrix completion as

$$\arg \min_{\mathbf{A}, \mathbf{B}} \|\mathbf{A}\|_p, \text{ s.t. } \mathbf{A} = \mathbf{B}, \mathcal{P}_\Omega(\mathbf{B}) = \mathcal{P}_\Omega(\mathbf{O}), \quad (25)$$

Fig. 20: Batch image alignment experiments. (a) Three input images. (b-d) The aligned, low-rank, sparse results from Peng *et al.* [38]. (e-g) The aligned, low-rank, sparse results from the proposed method.Fig. 21: Aligning planar surfaces despite occlusions by RASL [38] and ours with $n = 4$ images. Affine transformation is used as the geometric transformation model \mathbf{g} .Fig. 22: Close-up comparisons of Fig. 21 (see red box in the left) with the average images of aligned results $\mathbf{O} \circ \mathbf{g}$ and recovered low-rank components \mathbf{A} between RASL [38] and ours.



Index	1	2	3	4	5	6	7	8
PSNR [26]	30.428	21.741	24.506	32.282	24.375	42.145	33.357	21.293
Ours	30.429	21.768	24.507	32.216	24.376	42.011	33.282	21.325
Iter. [26]	755	727	631	761	639	678	1251	799
Ours	183	210	201	196	192	181	216	201
Time [26] (sec)	18.60	18.36	15.49	18.77	15.87	16.59	20.84	19.35
Ours	4.06	4.30	4.48	4.20	4.09	3.94	3.07	4.47

Fig. 23: Image recovery application. Top: Original images (ground truth). Middle: Observed images with 50% missing entries (input). Bottom: Recovered image by our method. Table: Quantitative comparison with Hu *et al.* [26] for PSNR, number of iteration, and running time.

where $\mathcal{P}_\Omega(\cdot)$ is the orthogonal projection operator setting $[\mathcal{P}_\Omega(\mathbf{X})]_{i,j} = [\mathbf{X}]_{i,j}$ for $(i,j) \in \Omega$ and 0 otherwise. Although the auxiliary variable \mathbf{B} looks trivial, but with the affine constraint (the projection operator) it make the efficient PSVT operator applicable in ADMM algorithm. We set $\rho = 1.05$ in ADMM (refer to the supplementary material and Alg. 1), and for fair comparison, we follow the same setting suggested by Hu *et al.*, i.e. $\mu_0 = 1e^{-3}$.

Fig. 23 shows the comparison with Hu *et al.* Since the proposed method has similar objective function with Hu *et al.*, PSNR of recovered images are similar, but our method requires fewer iterations and runs 4 times faster. Because Hu *et al.* locally approximate to solve PSSV, their algorithm requires outer loop to fix subspaces and inner loop to minimize nuclear norm with affine constraint. In contrast, our method directly minimizes PSSV, which is a key contribution of our work.

5 DISCUSSIONS AND CONCLUSION

In this paper, we revisited the rank minimization method in RPCA for low-level vision problems. When the target rank is known, we show that, by modifying the objective function from the nuclear norm to PSSV, we can achieve a better control of the target rank of the low-rank solution, even when the number of observations is limited. The appealing advantage of our solution is that it can be easily utilized in existing algorithms, e.g. ADMM [33], and the efficient computation properties still hold. The generality and the effectiveness of our approach are supported through numerous and extensive experiments on both synthetic examples and several real-world applications which outperform the conventional nuclear norm objective function. We do not consider scalability issues of our method in this paper, but the recent approach suggested by Oh *et al.* [37] allow to speed-up the application of our method. An interesting direction of future work is the mathematical analysis of the properties, e.g. the necessary and the sufficient conditions [39] of our partial sum objective function compared to the nuclear norm solution. In the following, we discuss some open questions related to our paper.

Sufficient number of samples versus minimum number of samples In our experimental analysis, we found that our solution is more robust than the nuclear norm solution when facing a limited number of samples. Defining K as the (theoretical) minimum number of samples for processing, e.g. 2 images for HDR, 3 images for photometric stereo, our approach requires more than K samples for a robust model estimation and outlier rejection. We believe that the number of needed additional samples depends on the problem setting, e.g. the shape of feature space or the distribution of the samples.

Target rank While our formulation implicitly encourages a target rank constraint in the resulting matrix, this constraint is not hardly enforced. We discuss here two possible scenarios that can produce the resulting matrix having a rank different from the target rank. The first scenario is when a very limited number of samples are observed. In such case, PSVT can produce a deficient rank lower than the target rank when the span of the observed samples is less than the target rank, but this case is a fundamental limitation of under-sampling rather than a conceptual limitation of our approach. Another scenario is due to too much noise (especially for Gaussian noise that does not follow the sparsity property) in the observed samples which results in large singular values in the residual ranks. In this case, a solution to satisfy the rank constraint is to increase τ in Eq. (17). When τ is equal to infinity, our PSVT solution is close to the result using singular value projection [29]. However, the projection method enforcing target rank could produce an over-fitting solution due to the mentioned noise effects.

REFERENCES

- [1] A. Agarwal, S. Negahban, and M. J. Wainwright. Noisy matrix decomposition via convex relaxation: Optimal rates in high dimensions. In *Proceedings of the 28th International Conference on Machine Learning (ICML)*, pages 1129–1136, 2011.
- [2] F. Bach, J. Mairal, and J. Ponce. Convex sparse matrix factorizations. *arXiv preprint arXiv:0812.1869*, 2008.
- [3] A. Bagirov, N. Karmitsa, and M. Makela. Nonconvex analysis. In *Introduction to Nonsmooth Optimization*, pages 61–116. Springer International Publishing, 2014.
- [4] R. Basri, D. Jacobs, and I. Kemelmacher. Photometric stereo with general, unknown lighting. *IJCV*, 2007.
- [5] S. Boyd, N. Parikh, E. Chu, B. Peleato, and J. Eckstein. Distributed optimization and statistical learning via the alternating direction method of multipliers. *Foundations and Trends® in Machine Learning*, 3(1):1–122, 2011.
- [6] C. Bregler, A. Hertzmann, and H. Biermann. Recovering non-rigid 3D shape from image streams. In *CVPR*, 2000.
- [7] L. G. Brown. A survey of image registration techniques. In *ACM Computing Surveys*, 1992.
- [8] R. Cabral, F. D. L. Torre, J. P. Costeira, and A. Bernardino. Unifying nuclear norm and bilinear factorization approaches for low-rank matrix decomposition. In *ICCV*, pages 2488–2495. IEEE, 2013.
- [9] J.-F. Cai, E. J. Candès, and Z. Shen. A singular value thresholding algorithm for matrix completion. *SIAM Journal on Optimization*, 2010.
- [10] E. Candès, X. Li, Y. Ma, and J. Wright. Robust principal component analysis? *Journal of the ACM*, 2011.
- [11] V. Chandrasekaran, S. Sanghavi, P. A. Parrilo, and A. S. Willsky. Rank-sparsity incoherence for matrix decomposition. *SIAM Journal on Optimization*, 2011.

- [12] K. Chen, H. Dong, and K.-S. Chan. Reduced rank regression via adaptive nuclear norm penalization. *Biometrika*, 2013.
- [13] A. Daniilidis, N. Hadjisavvas, and J.-E. Martinez-Legaz. An appropriate subdifferential for quasiconvex functions. *SIAM Journal on Optimization*, 12(2):407–420, 2002.
- [14] F. De la Torre and M. Black. Robust principal component analysis for computer vision. In *ICCV*, 2001.
- [15] F. De la Torre and M. Black. A framework for robust subspace learning. *IJCV*, 2003.
- [16] E. M. de Sá. Exposed faces and duality for symmetric and unitarily invariant norms. *Linear Algebra and its Applications*, 1994.
- [17] P. Debevec and J. Malik. Recovering high dynamic range radiance maps from photographs. In *ACM SIGGRAPH*, 1997.
- [18] D. L. Donoho. High-dimensional data analysis: the curses and blessings of dimensionality. In *American Mathematical Society Conf. Math Challenges of the 21st Century*, 2000.
- [19] D. L. Donoho and I. M. Johnstone. Adapting to unknown smoothness via wavelet shrinkage. *Journal of the american statistical association*, 90(432):1200–1224, 1995.
- [20] A. Eriksson and A. van den Hengel. Efficient computation of robust weighted low-rank matrix approximations using the l_1 norm. *IEEE Trans. on PAMI*, 2012.
- [21] M. Fischler and R. Bolles. Random sample consensus: A paradigm for model fitting with applications to image analysis and automated cartography. *Communications of the ACM*, 1981.
- [22] S. Gaïffas and G. Lecué. Weighted algorithms for compressed sensing and matrix completion. *arXiv preprint arXiv:1107.1638*, 2011.
- [23] O. Gallo, N. Gelfand, W. Chen, M. Tico, and K. Pulli. Artifact-free high dynamic range imaging. *ICCP*, 2009.
- [24] E. T. Hale, W. Yin, and Y. Zhang. Fixed-point continuation for l_1 -minimization: Methodology and convergence. *SIAM Journal on Optimization*, 2008.
- [25] H. Hayakawa. Photometric stereo under a light source with arbitrary motion. *Journal of the Optical Society of America A*, 1994.
- [26] Y. Hu, D. Zhang, J. Ye, X. Li, and X. He. Fast and accurate matrix completion via truncated nuclear norm regularization. *IEEE Trans. on PAMI*, 2013.
- [27] A. Hyvärinen, J. Hurri, and P. O. Hoyer. *Natural Image Statistics: A Probabilistic Approach to Early Computational Vision.*, volume 39. Springer, 2009.
- [28] S. Ikehata, D. Wipf, Y. Matsushita, and K. Aizawa. Robust photometric stereo using sparse regression. In *CVPR*, 2012.
- [29] P. Jain, R. Meka, and I. Dhillon. Guaranteed rank minimization via singular value projection. In *NIPS*, 2010.
- [30] H. Ji, C. Liu, Z. Shen, and Y. Xu. Robust video denoising using low rank matrix completion. In *CVPR*, 2010.
- [31] I. T. Jolliffe. Principal Component Analysis. In *Springer-Verlag*, 1986.
- [32] Q. Ke and T. Kanade. Robust l_1 norm factorization in the presence of outliers and missing data by alternative convex programming. In *CVPR*, 2005.
- [33] Z. Lin, M. Chen, and Y. Ma. The augmented Lagrange multiplier method for exact recovery of corrupted low-rank matrices. Technical Report UIUC-ENG-09-2215, UIUC, 2009.
- [34] T.-H. Oh, H. Kim, Y.-W. Tai, J.-C. Bazin, and I. S. Kweon. Partial sum minimization of singular values in rpca for low-level vision. In *JCCV*. IEEE, 2013.
- [35] T.-H. Oh, J.-Y. Lee, and I. S. Kweon. High dynamic range imaging by a rank-1 constraint. In *ICIP*, 2013.
- [36] T.-H. Oh, J.-Y. Lee, Y.-W. Tai, and I. S. Kweon. Robust high dynamic range imaging by rank minimization. *IEEE Trans. on PAMI*, 2014.
- [37] T.-H. Oh, Y. Matsushita, Y.-W. Tai, and I. S. Kweon. Fast randomized singular value thresholding for nuclear norm minimization. In *CVPR*. IEEE, 2015.
- [38] Y. Peng, A. Ganesh, J. Wright, W. Xu, and Y. Ma. RASL: Robust alignment by sparse and low-rank decomposition for linearly correlated images. *IEEE Trans. on PAMI*, 2012.
- [39] B. Recht, W. Xu, and B. Hassibi. Necessary and sufficient conditions for success of the nuclear norm heuristic for rank minimization. In *IEEE Conference on Decision and Control*, 2008.
- [40] Y. Shen, Z. Wen, and Y. Zhang. Augmented lagrangian alternating direction method for matrix separation based on low-rank factorization. *Optimization Methods and Software*, 29(2):239–263, 2014.
- [41] C. Tomasi and T. Kanade. Shape and motion from image streams under orthography: a factorization method. *IJCV*, 1992.
- [42] R. Woodham. Photometric method for determining surface orientation from multiple images. In *Optical Engineering*, 1980.
- [43] J. Wright, A. Ganesh, S. Rao, and Y. Ma. Robust principal component analysis: Exact recovery of corrupted low-rank matrices via convex optimization. In *NIPS*, 2009.
- [44] J. Wright, A. Ganesh, Z. Zhou, K. Min, S. Rao, Z. Lin, Y. Peng, M. Chen, L. Wu, Y. Ma, E. Candès, and X. Li. Low-rank matrix recovery and completion via convex optimization. <http://perception.csl.illinois.edu/matrix-rank/home.html>.
- [45] B. Wu, C. Ding, D. Sun, and K.-C. Toh. On the moreau-yosida regularization of the vector k -norm related functions. *SIAM Journal on Optimization*, 24(2):766–794, 2014.
- [46] L. Wu, A. Ganesh, B. Shi, Y. Matsushita, Y. Wang, and Y. Ma. Robust photometric stereo via low-rank matrix completion and recovery. In *ACCV*, 2010.
- [47] Y. Wu and D. P. Wipf. Dual-space analysis of the sparse linear model. In *NIPS*, pages 1745–1753, 2012.
- [48] Z. Zhang, A. Ganesh, X. Liang, and Y. Ma. TILT: Transform invariant low-rank textures. *IJCV*, 2012.
- [49] Y. Zheng, G. Liu, S. Sugimoto, S. Yan, and M. Okutomi. Practical low-rank matrix approximation under robust l_1 -norm. In *CVPR*, 2012.
- [50] Z. Zhou, X. Li, J. Wright, E. Candès, and Y. Ma. Stable principal component pursuit. In *IEEE International Symposium on Information Theory Proceedings (ISIT)*, pages 1518–1522. IEEE, 2010.

Supplementary Material: Partial Sum Minimization of Singular Values in Robust PCA: Algorithm and Applications

Tae-Hyun Oh *Student Member, IEEE*, Yu-Wing Tai *Senior Member, IEEE*,
Jean-Charles Bazin *Member, IEEE*, Hyeonwoo Kim *Student Member, IEEE*,
and In So Kweon *Member, IEEE*



SUPPLEMENTARY MATERIAL

In this supplementary material, we prove Proposition 1, and the pseudo code of the algorithm of image recovery application is provided. We also present an additional experimental result not included in the main paper due to space limitation. All the parameters are same as in the main paper or the referred papers, except if state otherwise.

1 PROOFS

Lemma 4 (Lipschitz continuous of PSSV). *The function of the partial sum of singular values $h(\mathbf{X}) = \|\mathbf{X}\|_p$ for $\mathbf{X} \in \mathbb{R}^{m \times n}$ is Lipschitz continuous. Namely, there exists a constant K satisfying*

$$|h(\mathbf{X}_1) - h(\mathbf{X}_2)| \leq K \cdot \|\mathbf{X}_1 - \mathbf{X}_2\|_F.$$

Proof. Let the nuclear norm be $f(\mathbf{X}) = \|\mathbf{X}\|_*$, the Ky-Fan p -norm be $g(\mathbf{X}) = \|\mathbf{X}\|_{Ky(p)}$ for simplicity. We know that $h(\mathbf{X}) = \|\mathbf{X}\|_p = f(\mathbf{X}) - g(\mathbf{X})$, and the nuclear norm $f(\cdot)$ and the Ky-Fan p -norm $g(\cdot)$ are Lipschitz continuous [33], [42], so we have

$$\begin{aligned} |f(\mathbf{X}_1) - f(\mathbf{X}_2)| &\leq K_f \cdot \|\mathbf{X}_1 - \mathbf{X}_2\|_F \\ |g(\mathbf{X}_1) - g(\mathbf{X}_2)| &\leq K_g \cdot \|\mathbf{X}_1 - \mathbf{X}_2\|_F \end{aligned} \quad (26)$$

We see that

$$\begin{aligned} |h(\mathbf{X}_1) - h(\mathbf{X}_2)| &= |f(\mathbf{X}_1) - g(\mathbf{X}_1) - (f(\mathbf{X}_2) - g(\mathbf{X}_2))| \\ &= |f(\mathbf{X}_1) - f(\mathbf{X}_2) + (g(\mathbf{X}_2) - g(\mathbf{X}_1))| \\ &\leq |f(\mathbf{X}_1) - f(\mathbf{X}_2)| + |g(\mathbf{X}_1) - g(\mathbf{X}_2)| \quad (\text{by triangle inequality}) \\ &\leq (K_f + K_g) \cdot \|\mathbf{X}_1 - \mathbf{X}_2\|_F. \end{aligned}$$

Since the constant $K = K_f + K_g$ satisfy the inequality, $\|\cdot\|_p$ is Lipschitz continuous. \square

Since PSSV $\|\cdot\|_p$ is a non-convex function, so the typical subdifferential for convex functions (Fenchel-Moreau subdifferential for convex functions. Refer to Daniilidis *et al.* [13]) would be empty set. Therefore, we introduce a generalized subdifferential (or Clarke subdifferential) [3] for non-convex locally Lipschitz continuous functions.

Definition 2 (Generalized subgradients). *Let $f : \mathbb{R}^n \rightarrow \mathbb{R}$ be a locally Lipschitz continuous function at a point $\mathbf{x} \in \mathbb{R}^n$. Then the subdifferential of f at \mathbf{x} is the set $\partial_C f(\mathbf{x})$ of vectors $\mathbf{z} \in \mathbb{R}^n$ such that*

$$\partial_C f(\mathbf{x}) = \{\mathbf{z} : f^\circ(\mathbf{x}; \mathbf{d}) \geq \langle \mathbf{z}, \mathbf{d} \rangle \text{ for all } \mathbf{d} \in \mathbb{R}^n\}, \quad (27)$$

where the directional subgradient with respect to the direction vector \mathbf{d} is defined $f^\circ(\mathbf{x}; \mathbf{d}) = \limsup_{\substack{\mathbf{y} \rightarrow \mathbf{x} \\ t \downarrow 0}} \frac{f(\mathbf{y} + t\mathbf{d}) - f(\mathbf{y})}{t}$. Each vector $\mathbf{z} \in \partial_C f(\mathbf{x})$ is again called a subgradient of f at \mathbf{x} .

Remark D.2.1 Definition 2 can be generalized to matrix cases analogously.

Remark D.2.2 Regardless of non-convexity or non-smoothness, the generalized subdifferential (here, Clarke subdifferential) always exists for locally Lipschitz continuous functions. Also, $\partial_C \|\cdot\|_p$ is well defined in $\mathbb{R}^{m \times n}$, because $\|\cdot\|_p$ is a Lipschitz continuous function as in Lemma 4.

Remark D.2.3 Basic properties of the generalized subdifferential are identical to those in convex case, and most of subdifferential calculus rules hold. Note that Karush-Kuhn-Tucker (KKT) optimality conditions is also properly defined with the generalized subdifferential [3].

Proposition 1 (Convergence). Let $S_k = (\mathbf{A}_k, \mathbf{E}_k, \mathbf{Y}_k, \hat{\mathbf{Y}}_k)$, where $\hat{\mathbf{Y}}_{k+1} = \mathbf{Y}_k + \mu_k(\mathbf{O} - \mathbf{A}_{k+1} - \mathbf{E}_k)$ and $\{S_k\}_{k=1}^\infty$ be generated by Algorithm 1. Suppose that $\{\mathbf{Y}_k\}_{k=1}^\infty, \{\hat{\mathbf{Y}}_k\}_{k=1}^\infty$ are bounded, $\lim_{k \rightarrow \infty} (\mathbf{Y}_{k+1} - \mathbf{Y}_k) = \mathbf{0}$, and μ_k is non-decreasing, then any accumulation point of $\{S_k\}_{k=1}^\infty$ satisfies the following KKT conditions,

$$(C1) \mathbf{Y}^* \in \partial_C \|\mathbf{A}^*\|_p, \quad (C2) \mathbf{Y}^* \in \partial \|\lambda \mathbf{E}^*\|_1, \quad (C3) \mathbf{O} - \mathbf{A}^* - \mathbf{E}^* = \mathbf{0}, \quad (C4) \partial_C \|\mathbf{A}^*\|_p \cap \partial \|\lambda \mathbf{E}^*\|_1 \neq \emptyset. \quad (28)$$

In particular, whenever $\{S_k\}_{k=1}^\infty$ converges, it converges to a KKT point of Eq. (2) of the main paper.

Proof. For \mathbf{Y} , we have $\mu_k^{-1}(\mathbf{Y}_{k+1} - \mathbf{Y}_k) = \mathbf{O} - \mathbf{A}_{k+1} - \mathbf{E}_{k+1}$. By our assumptions, $\lim_{k \rightarrow \infty} (\mathbf{Y}_{k+1} - \mathbf{Y}_k) = \mathbf{0}$ and μ_k is non-decreasing, $\mathbf{O} - \mathbf{A}_{k+1} - \mathbf{E}_{k+1} = \mu_k^{-1}(\mathbf{Y}_{k+1} - \mathbf{Y}_k) \rightarrow \mathbf{0}$, which satisfies (C3).

Since \mathbf{E}_{k+1} obtained by the soft-thresholding operator [9] minimizes $L_{\mu_k}(\mathbf{A}_{k+1}, \mathbf{E}, \mathbf{Y}_k)$ by definition, we have

$$\begin{aligned} \mathbf{0} &\in \partial \|\lambda \mathbf{E}_{k+1}\|_1 - \mathbf{Y}_k - \mu_k(\mathbf{O} - \mathbf{A}_{k+1} - \mathbf{E}_{k+1}) \\ &= \partial \|\lambda \mathbf{E}_{k+1}\|_1 - \mathbf{Y}_{k+1} \\ &\quad (\text{Since } \mathbf{Y}_{k+1} = \mathbf{Y}_k + \mu_k(\mathbf{O} - \mathbf{A}_{k+1} - \mathbf{E}_{k+1})) \\ &\Rightarrow \mathbf{Y}_{k+1} \in \partial \|\lambda \mathbf{E}_{k+1}\|_1, \end{aligned} \quad (29)$$

which satisfies (C2).

Since \mathbf{A}_{k+1} optimally obtained by the PSVT minimizes $L_{\mu_k}(\mathbf{A}, \mathbf{E}_k, \mathbf{Y}_k)$ by Theorem 1, we have

$$\begin{aligned} \mathbf{0} &\in \partial_C \|\mathbf{A}_{k+1}\|_p - \mathbf{Y}_k - \mu_k(\mathbf{O} - \mathbf{A}_{k+1} - \mathbf{E}_k) \\ &= \partial_C \|\mathbf{A}_{k+1}\|_p - \mathbf{Y}_k - \mu_k(\mathbf{O} - \mathbf{A}_{k+1} - \mathbf{E}_{k+1}) - \mu_k(\mathbf{E}_{k+1} - \mathbf{E}_k) \\ &= \partial_C \|\mathbf{A}_{k+1}\|_p - \mathbf{Y}_{k+1} - \mu_k(\mathbf{E}_{k+1} - \mathbf{E}_k) \\ &\Rightarrow \mathbf{Y}_{k+1} + \mu_k(\mathbf{E}_{k+1} - \mathbf{E}_k) \in \partial_C \|\mathbf{A}_{k+1}\|_p. \end{aligned} \quad (30)$$

By the assumption that $\{\mathbf{Y}_k\}_{k=1}^\infty, \{\hat{\mathbf{Y}}_k\}_{k=1}^\infty$ are bounded, there must exist $c > 0$ such that $\|\mathbf{Y}_{k+1}\|_F \leq c, \|\hat{\mathbf{Y}}_{k+1}\|_F \leq c$. Then,

$$\begin{aligned} \mathbf{Y}_{k+1} - \hat{\mathbf{Y}}_{k+1} &= \mu_k (\mu_k^{-1}(\mathbf{Y}_{k+1} - \mathbf{Y}_k) - (\mathbf{O} - \mathbf{A}_{k+1} - \mathbf{E}_k)) \\ &= \mu_k ((\mathbf{O} - \mathbf{A}_{k+1} - \mathbf{E}_{k+1}) - (\mathbf{O} - \mathbf{A}_{k+1} - \mathbf{E}_k)) = \mu_k(\mathbf{E}_k - \mathbf{E}_{k+1}) \\ &\Rightarrow \|\mathbf{E}_{k+1} - \mathbf{E}_k\|_F = \mu_k^{-1} \|\mathbf{Y}_{k+1} - \hat{\mathbf{Y}}_{k+1}\|_F \\ &\leq \mu_k^{-1} (\|\mathbf{Y}_{k+1}\|_F + \|\hat{\mathbf{Y}}_{k+1}\|_F) \quad (\text{by triangle inequality}) \\ &\leq 2c\mu_k^{-1} \rightarrow 0 \quad (\text{since } \mu_k \text{ is non-decreasing}). \end{aligned} \quad (31)$$

Thus, $\mathbf{Y}_{k+1} \rightarrow \mathbf{Y}^* \in \partial_C \|\mathbf{A}^*\|_p$ from Eq. (30) and $\mathbf{Y}^* \in \partial_C \|\mathbf{A}^*\|_p \cap \partial \|\lambda \mathbf{E}^*\|_1 \neq \emptyset$ which satisfy (C1) and (C4). The sequence $\{S_k\}_{k=1}^\infty$ gradually satisfies the KKT conditions, which completes the proof. \square

Remark P.1.1 In Alg. 1, the assumption for μ_k is always satisfied by the update rule $\mu_{k+1} = \rho\mu_k$ ($\rho > 1$), and the boundness of the sequence $\{\mathbf{Y}_k\}_{k=1}^\infty, \{\hat{\mathbf{Y}}_k\}_{k=1}^\infty$ are satisfied by Lemma 1 of Lin et al. [33] and Lemma 5 and 6 in the below. Also, $\lim_{k \rightarrow \infty} \|\mathbf{Y}_{k+1} - \mathbf{Y}_k\|_F = 0$ could be proved in the same manner with the proof of Theorem 2 of Lin et al. [33], which is based on a saddle point analysis. Therefore, we see that Alg. 1 converge as long as \mathbf{Y}_k is converged.

Lemma 5 (Boundness of $|f^\circ(\cdot; \cdot)|$) [3] Let $f : \mathbb{R}^{m \times n} \rightarrow \mathbb{R}$ be a locally Lipschitz continuous function at \mathbf{X} with constant K , and $\mathbf{d} \in \mathbb{R}^{m \times n}$. Then,

$$|f^\circ(\mathbf{X}; \mathbf{d})| \leq B \|\mathbf{d}\|_F. \quad (32)$$

Proof. Refer to the proof of Theorem 3.1 in [3]. \square

Lemma 6 (Boundness of Clarke subgradient) *Let $f : \mathbb{R}^{m \times n} \rightarrow \mathbb{R}$ be a locally Lipschitz continuous function at \mathbf{X} with constant K , and $\mathbf{d} \in \mathbb{R}^{m \times n}$. Then, a subgradient $\mathbf{Y} \in \partial_C f(\mathbf{X})$ is bounded as*

$$\|\mathbf{Y}\|_F \leq B, \quad (33)$$

where B is the same constant in Lemma 5.

Proof. By the definition of the Clarke subdifferential, \mathbf{Y} satisfies $f^\circ(\mathbf{X}; \mathbf{d}) \geq \langle \mathbf{Y}, \mathbf{d} \rangle$ for all $\mathbf{d} \in \mathbb{R}^{m \times n}$. By setting $\mathbf{d} = \mathbf{Y}$, we get $f^\circ(\mathbf{X}; \mathbf{Y}) \geq \langle \mathbf{Y}, \mathbf{Y} \rangle = \|\mathbf{Y}\|_F^2$. Then, by Lemma 5, we have

$$\begin{aligned} \|\mathbf{Y}\|_F^2 &\leq |f^\circ(\mathbf{X}; \mathbf{Y})| \leq B \|\mathbf{Y}\|_F \\ \Rightarrow \|\mathbf{Y}\|_F^2 &\leq B \|\mathbf{Y}\|_F \\ \Rightarrow \|\mathbf{Y}\|_F &\leq B \end{aligned} \quad (34)$$

□

2 ALGORITHM FOR IMAGE RECOVERY

Algorithm 2 ADMM for Image Recovery

Input : $\mathbf{O} \in \mathbb{R}^{m \times n}$, the index map Ω , the constraint rank N .
Initialize $\mathbf{A}_0 = \mathbf{O}$, $\mathbf{B}_0 = \mathbf{Z}_0 = \mathbf{0}$, $\mu_0 > 0$, $\rho > 1$ and $k = 0$.
while not converged **do**
 $\mathbf{A}_{k+1} = \mathbb{P}_{N, \mu_k^{-1}}[\mathbf{B}_k - \mu_k^{-1} \mathbf{Z}_k]$.
 $\mathbf{B}_{k+1} = \arg \min_{\mathcal{P}_\Omega(\mathbf{B}) = \mathcal{P}_\Omega(\mathbf{O})} \|\mathbf{B} - (\mathbf{A}_{k+1} + \mu_k^{-1} \mathbf{Z}_k)\|_F^2$.
 $\mathbf{Z}_{k+1} = \mathbf{Z}_k + \mu_k (\mathbf{A}_{k+1} - \mathbf{B}_{k+1})$.
 $\mu_{k+1} = \rho \mu_k$.
 $k = k + 1$.
end while
Output : \mathbf{A}_k .

3 AN ADDITIONAL RESULTS

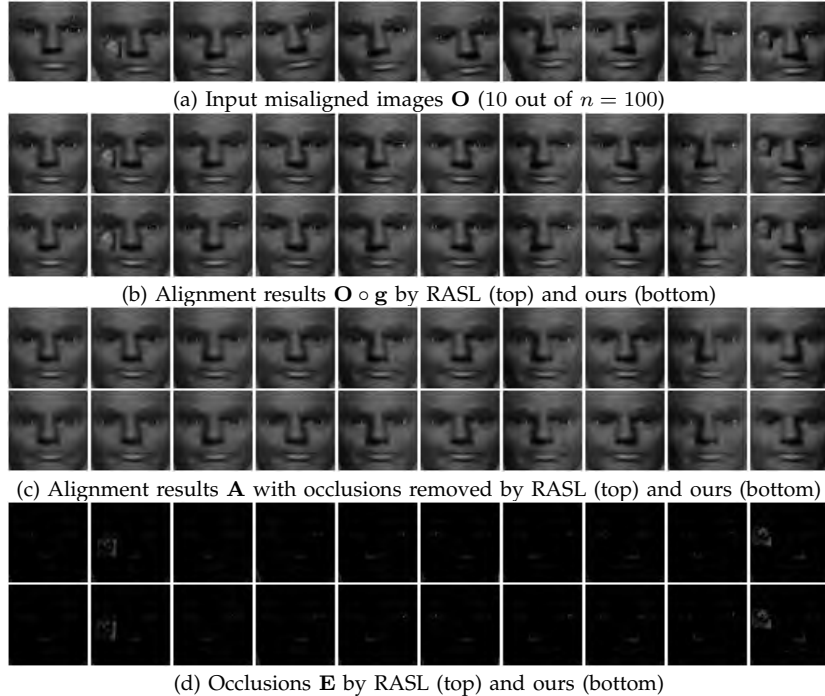


Fig. 25: Results of the batch image alignment by RASL [35] and ours for $n = 100$ input images. Similarity transformation is used as geometric transformation model \mathbf{g} . This shows that our method performs identically to conventional RPCA with many samples. This result is consistent with the results with synthetic data in Sec. 4.1 of the main paper.